Cosmological simulations with self-interacting dark matter – I. Constant-density cores and substructure

Miguel Rocha,[1][*] Annika H. G. Peter,[1] James S. Bullock,[1] Manoj Kaplinghat,[1] Shea Garrison-Kimmel,[1] Jose Oñorbe[1] and Leonidas A. Moustakas[2]

[1]*Center for Cosmology, Department of Physics and Astronomy, University of California, Irvine, CA 92697-4575, USA*
[2]*Jet Propulsion Laboratory, California Institute of Technology, Pasadena, CA 91109, USA*

ABSTRACT

We use cosmological simulations to study the effects of self-interacting dark matter (SIDM) on the density profiles and substructure counts of dark-matter haloes from the scales of spiral galaxies to galaxy clusters, focusing explicitly on models with cross-sections over dark-matter particle mass $\sigma/m = 1$ and $0.1\,\mathrm{cm}^2\,\mathrm{g}^{-1}$. Our simulations rely on a new SIDM *N*-body algorithm that is derived self-consistently from the Boltzmann equation and that reproduces analytic expectations in controlled numerical experiments. We find that well-resolved SIDM haloes have constant-density cores, with significantly lower central densities than their cold dark matter (CDM) counterparts. In contrast, the subhalo content of SIDM haloes is only modestly reduced compared to CDM, with the suppression greatest for large hosts and small halo-centric distances. Moreover, the large-scale clustering and halo circular velocity functions in SIDM are effectively identical to CDM, meaning that all of the large-scale successes of CDM are equally well matched by SIDM. From our largest cross-section runs, we are able to extract scaling relations for core sizes and central densities over a range of halo sizes and find a strong correlation between the core radius of an SIDM halo and the NFW scale radius of its CDM counterpart. We construct a simple analytic model, based on CDM scaling relations, that captures all aspects of the scaling relations for SIDM haloes. Our results show that halo core densities in $\sigma/m = 1\,\mathrm{cm}^2\,\mathrm{g}^{-1}$ models are too low to match observations of galaxy clusters, low surface brightness spirals (LSBs) and dwarf spheroidal galaxies. However, SIDM with $\sigma/m \simeq 0.1\,\mathrm{cm}^2\,\mathrm{g}^{-1}$ appears capable of reproducing reported core sizes and central densities of dwarfs, LSBs and galaxy clusters without the need for velocity dependence. Higher resolution simulations over a wider range of masses will be required to confirm this expectation. We discuss constraints arising from the Bullet cluster observations, measurements of dark-matter density on small scales and subhalo survival requirements, and show that SIDM models with $\sigma/m \simeq 0.1\,\mathrm{cm}^2\,\mathrm{g}^{-1} \simeq 0.2\,\mathrm{barn}\,\mathrm{GeV}^{-1}$ are consistent with all observational constraints.

Key words: methods: numerical – galaxies: haloes – dark matter.

1 INTRODUCTION

There is significant evidence that some form of dark matter dominates the gravitating mass in the Universe and its abundance is known to great precision (Komatsu et al. 2011). The most popular candidate for dark matter is the class of weakly interacting massive particles (WIMPs), of which supersymmetric neutralinos are examples (Steigman & Turner 1985; Griest 1988; Jungman, Kamionkowski & Griest 1996). WIMPs are stable, with negligible self-interactions, and are non-relativistic at decoupling ('cold').

It is important to recognize that of these characteristics, it is primarily their coldness that is well tested via its association with significant small-scale power. Indeed, WIMPs are the canonical cold dark matter (CDM) candidate. Cosmological models based on CDM reproduce the spatial clustering of galaxies on large scales quite well (Reid et al. 2010) and even the clustering of galaxies on ∼1 Mpc scales appears to match that expected for CDM *subhaloes* (Kravtsov et al. 2004; Conroy, Wechsler & Kravtsov 2006; Trujillo-Gomez et al. 2011; Reddick et al. 2012).

Beyond the fact that the Universe appears to behave as expected for CDM on large scales, we have few constraints on the microphysical parameters of the dark matter, especially those that would manifest themselves at the high densities associated with cores of

[*] E-mail: rocham@uci.edu

galaxy haloes. It is worth asking what (if anything) about vanilla CDM can change without violating observational bounds. In this paper, we use cosmological simulations to explore the observational consequences of a CDM particle that is strongly self-interacting, focusing specifically on the limiting case of velocity-independent, elastic scattering.

Dark-matter particles with appreciable self-interactions have been discussed in the literature for more than two decades (Carlson, Machacek & Hall 1992; Machacek, Carlson & Hall 1993; de Laix, Scherrer & Schaefer 1995; Firmani et al. 2000; Spergel & Steinhardt 2000), and are now recognized as generic consequences of hidden-sector extensions to the Standard Model (Pospelov, Ritz & Voloshin 2008; Ackerman et al. 2009; Arkani-Hamed et al. 2009; Feng et al. 2009; Feng, Kaplinghat & Yu 2010; Loeb & Weiner 2011). Importantly, even if dark sector particles have no couplings to Standard Model particles they might experience strong interactions with themselves, mediated by dark gauge bosons (see Feng 2010; Peter 2012 for reviews). *The implication is that astrophysical constraints associated with the small-scale clustering of dark matter may be the only way to test these scenarios.*

Phenomenologically, self-interacting dark matter (SIDM) is attractive because it offers a means to lower the central densities of galaxies without destroying the successes of CDM on large scales. Cosmological simulations that contain only CDM indicate that dark-matter haloes should be cuspy and with (high) concentrations that correlate with the collapse time of the halo (Navarro, Frenk & White 1997; Bullock et al. 2001; Wechsler et al. 2002). This is inconsistent with observations of galaxy rotation curves, which show that galaxies are less concentrated and less cuspy than predicted in CDM simulations (e.g. Flores & Primack 1994; Salucci & Burkert 2000; Gentile et al. 2004; Simon et al. 2005; Kuzio de Naray, McGaugh & de Blok 2008; de Blok 2010; Dutton et al. 2011; Kuzio de Naray & Spekkens 2011; Oh et al. 2011a; Walker & Peñarrubia 2011; Castignani et al. 2012; Salucci et al. 2012). Even for clusters of galaxies, the density profiles of the host dark-matter haloes appear in a number of cases to be shallower than predicted by CDM-only structure simulations, with the total (dark matter + baryons) density profile in a closer match to the CDM prediction for the dark matter alone (e.g. Sand et al. 2004, 2008; Newman et al. 2009, 2011; Coe et al. 2012; Umetsu et al. 2012).

One possible answer is feedback. In principle, the expulsion of gas from galaxies can result in lower dark-matter densities compared to dissipationless simulations, and thus bring CDM models in line with observations (Governato et al. 2010; Oh et al. 2011b; Pontzen & Governato 2012; Brook et al. 2012; Governato et al. 2012). However, a new level of concern exists for dwarf spheroidal (dSph) galaxies (Boylan-Kolchin, Bullock & Kaplinghat 2011, 2013; Ferrero et al. 2012). Systems with $M_* \sim 10^6\,\mathrm{M_\odot}$ appear to be missing $\sim 5 \times 10^7\,\mathrm{M_\odot}$ of dark matter compared to standard CDM expectations (Boylan-Kolchin et al. 2012). It is difficult to understand how feedback from such a tiny amount of star formation could have possibly blown out enough gas to reduce the densities of dSph galaxies to the level required to match observations (Boylan-Kolchin et al. 2012; Peñarrubia et al. 2012; Teyssier et al. 2012; Zolotov et al. 2012; Garrison-Kimmel et al., in preparation).

Spergel & Steinhardt (2000) were the first to discuss SIDM in the context of the central density problem (see also Firmani et al. 2000). The centres of SIDM haloes are expected to have constant-density isothermal cores that arise as kinetic energy is transmitted from the hot outer halo inward (Balberg, Shapiro & Inagaki 2002; Colín et al. 2002; Ahn & Shapiro 2005; Koda & Shapiro 2011). This can happen if the cross-section over mass of the dark-matter particle,

σ/m, is large enough for there to be a relatively high probability of scattering over a time t_age comparable to the age of the halo: $\Gamma\, t_\mathrm{age} \sim 1$, where Γ is the scattering rate per particle. The rate will vary with local dark-matter density $\rho(r)$ as a function of radius r in a dark halo as

$$\Gamma(r) \simeq \rho(r)(\sigma/m)v_\mathrm{rms}(r), \tag{1}$$

up to order unity factors, where v_rms is the rms speed of dark-matter particles. Based on rough analytic arguments, Spergel & Steinhardt (2000) suggested that $\sigma/m \sim 0.1\text{–}100\ \mathrm{cm^2\,g^{-1}}$ would produce observable consequences in the cores of haloes.

Numerical simulations have confirmed the expected phenomenology of core formation (Burkert 2000) though Kochanek & White (2000) emphasized the possibility that SIDM haloes could eventually become *more* dense than their CDM counterparts as a result of eventual heat flux from the inside out (much like core-collapse globular clusters). However, this process is suppressed when merging from hierarchical formation is included (for a discussion see Ahn & Shapiro 2005). We do not see clear signatures of core collapse in the haloes we analysed for $\sigma/m = 1\ \mathrm{cm^2\,g^{-1}}$.

The first cosmological simulations aimed at understanding dwarf densities were performed by Davé et al. (2001) who used a small volume ($4\,h^{-1}$ Mpc on a side) in order to focus computational power on dwarf haloes. They concluded that $\sigma/m = 0.1\text{–}10\,\mathrm{cm^2\,g^{-1}}$ came close to reproducing core densities of small galaxies, favouring the upper end of that range but not being able to rule out the lower end due to resolution. Almost concurrently, Yoshida et al. (2000) ran cosmological simulations focusing on the cluster-mass regime. Based on the estimated core size of cluster CL 0024+1654, they concluded that cross-sections no larger than $\sim 0.1\ \mathrm{cm^2\,g^{-1}}$ were allowed, raising doubts that constant-cross-section SIDM models could be consistent with observations of both dwarf galaxies and clusters.

These concerns were echoed by Miralda-Escudé (2002) who suggested that SIDM haloes would be significantly more spherical than observed for galaxy clusters. Similarly, Gnedin & Ostriker (2001) argued that SIDM would lead to excessive subhalo evaporation in galaxy clusters. More recently, the merging cluster system known as the Bullet cluster has been used to derive the limits (68 per cent C.L.) $\sigma/m < 0.7\ \mathrm{cm^2\,g^{-1}}$ (Randall et al. 2008) based on evaporation of dark matter from the subcluster and $\sigma/m < 1.25\ \mathrm{cm^2\,g^{-1}}$ (Randall et al. 2008) based on the observed lack of offset between the Bullet subcluster mass peak and the galaxy light centroid. In order to relax this apparent tension between what was required to match dwarf densities and the observed properties of galaxy clusters, velocity-dependent cross-sections that diminish the effects of self-interaction in cluster environments have been considered (Firmani et al. 2000; Colín et al. 2002; Feng et al. 2009; Loeb & Weiner 2011; Vogelsberger, Zavala & Loeb 2012).

There are a few new developments that motivate us to revisit constant SIDM cross-sections of the order of $\sigma/m \sim 1\ \mathrm{cm^2\,g^{-1}}$. For example, the cluster (CL 0024+1654) used by Yoshida et al. (2000) to place one of the tightest limits at $\sigma/m = 0.1$ is now recognized as an ongoing merger along the line of sight (Czoske et al. 2001, 2002; Zhang et al. 2005; Jee et al. 2007; Jee 2010; Umetsu et al. 2010). This calls into question its usefulness as a comparison case for non-merging cluster simulations. In a companion paper (Peter et al. 2012), we use the same simulations described here to show that published constraints on SIDM based on halo shape comparisons are significantly weaker than previously believed. Further, the results presented below clearly demonstrate that the tendency for subhaloes to evaporate in SIDM models (Gnedin & Ostriker 2001)

is not significant for $\sigma/m \sim 1\,\mathrm{cm^2\,g^{-1}}$. Finally (and related to the previous point), the best numerical analysis of the Bullet cluster (Randall et al. 2008) used initial cluster density profiles that were unmotivated cosmologically with central densities about a factor of 2 too high for the SIDM cross-sections considered (producing a scattering rate that is inconsistently high). Based on this observation, the Bullet cluster constraint based on evaporation of dark matter from the subcluster should be relaxed since the amount of subcluster mass that becomes unbound is directly proportional to the density of dark matter encountered in its orbit. Moreover, their model galaxies were placed in the cluster halo potentials without subhaloes surrounding them, an assumption (based on analytic estimates for SIDM subhalo evaporation) that is not supported by our simulations. This could affect the constraints based on the (lack of) offset between dynamical mass and light. Thus, we believe that the Bullet cluster constraints as discussed above are likely only relevant for models with $\sigma/m > 1\,\mathrm{cm^2\,g^{-1}}$. However, the constraints could be made significantly stronger by comparing SIDM predictions to the densities inferred from the convergence maps since the central halo densities for $\sigma/m \simeq 1\,\mathrm{cm^2\,g^{-1}}$ are significantly lower than the CDM predictions, as we show later.

Given these motivations, we perform a set of cosmological simulations with both CDM and SIDM. For SIDM we ran $\sigma/m = 1$ and $0.1\,\mathrm{cm^2\,g^{-1}}$ models (hereafter SIDM$_1$ and SIDM$_{0.1}$, respectively), i.e. models that we have argued pass the Bullet cluster tests. Our simulations provide us with a sample of haloes that span a mass range much larger than either Davé et al. (2001) or Yoshida et al. (2000) both with and without self-interactions.

One of the key findings from our simulations is that the core sizes are expected to scale approximately as a fixed fraction of the NFW scale radius the halo would have in the absence of scatterings. We can see where this scaling arises from a quick look at equation (1). This equation allows us to argue that the radius (r_1) below which we expect dark-matter particles (on average) to have scattered once or more is set by

$$\rho_s f(r/r_s) v_{\mathrm{rms}} \propto \frac{V_{\mathrm{max}}^2}{r_{\mathrm{max}}^2} f(r_1/r_s) V_{\mathrm{max}} = \mathrm{constant}, \qquad (2)$$

where $f(x)$ is the functional form of the NFW (or a related) density profile, r_{max} is the radius at which the circular velocity peaks and V_{max} is the maximum circular velocity. In writing the above equation we have assumed that the density profile for SIDM is not significantly different from CDM at r_1, something that we verify through our simulations. Now, since CDM enforces a $V_{\mathrm{max}} - r_{\mathrm{max}}$ relation such that $V_{\mathrm{max}} \propto r_{\mathrm{max}}^{1.4} - r_{\mathrm{max}}^{1.5}$, we see that the solution to r_1/r_s is going to be only mildly dependent on the halo properties. We develop an analytic model based on this insight later, but this is the underlying reason for why we find core sizes to be a fixed fraction of the NFW scale radius of the same halo in the absence of scatterings.

The major conclusion we reach based on the simulations and the analytic model presented here is that an SIDM model with a cross-section over dark-matter particle mass $\sim 0.1\,\mathrm{cm^2\,g^{-1}}$ would be capable of reproducing the core sizes and central densities observed in dark-matter haloes *at all scales*, from clusters to dSphs, without the need for velocity dependence in the cross-section.

In the next section, we discuss our new algorithm to compute the self-interaction probability for N-body particles, derived self-consistently from the Boltzmann equation. We discuss this new algorithm in detail in Appendix A. In Section 2, we show how this algorithm is implemented in the publicly available code GADGET2 (Springel 2005). We run tests that show that our algorithm gets the correct interaction rate and post-scattering kinematics. The results of these tests are given in Section 3. The cosmological simulations with this new algorithm are described in detail in Section 4. In Section 5.1 we provide some preliminary illustrations of our simulation snapshots, and in Section 5.2 we demonstrate that the large-scale statistical properties of SIDM are identical to CDM. In Section 5.4 we present the properties of individual SIDM$_1$ and SIDM$_{0.1}$ haloes and compare them to their CDM counterparts. In Section 5.4 we discuss the subhalo mass functions in our SIDM and CDM simulations and show that SIDM$_1$ subhalo mass functions are very close to that of CDM in the range of halo masses we can resolve. We provide scaling relations for the SIDM$_1$ halo properties in Section 6, and in Section 7 we present an analytic model that reproduces these scaling relations as well as the absolute densities and core radii of SIDM$_1$ haloes. We use these scaling relations and the analytic model to make a broad-brush comparison to observed data in Section 8. We present a summary together with our final conclusions in Section 9.

2 SIMULATING DARK MATTER SELF-INTERACTIONS

Our simulations rely on a new algorithm for modelling SIDM with N-body simulations. Here we introduce our approach and provide a brief summary. In Appendix A, we derive the algorithm explicitly starting with the Boltzmann equation and give details for general implementation.

In N-body simulations, the simulated (macro)particles represent an ensemble of many dark-matter particles. Each simulation particle of mass m_p can be thought of as a patch of dark-matter phase-space density. In our treatment of dark matter self-scattering, the phase-space patch of each particle is represented by a delta function in velocity and a spatially extended kernel $W(r, h_{\mathrm{si}})$, smoothing out the phase space in configuration space on a self-interaction smoothing length h_{si}. The value of h_{si} needs to be set by considering the physical conditions of the problem (see Section 3) as it specifies the range over which N-body particles can affect each other via self-interactions. In principle, h_{si} could be different for each particle and vary depending on the local density, but in the simulations presented here we fix h_{si} to be the same for all particles in a given simulation, setting the size of h_{si} according to the lowest densities at which self-interactions are effective for a given cross-section.

When two phase-space patches overlap in configuration space, we need to calculate the pairwise interaction rate between them. We do so by considering the 'scattering out' part of the Boltzmann collision term in equation (A1) and equations (A8)–(A13). The implied rate of scattering of an N-body particle j off of a target particle i of mass m_p is

$$\Gamma(i|j) = (\sigma/m) m_p |\boldsymbol{v}_i - \boldsymbol{v}_j| g_{ji}, \qquad (3)$$

where g_{ji} is a number density factor that accounts for the overlap of the two particles' smoothing kernels:[1]

$$g_{ji} = \int_0^{h_{\mathrm{si}}} \mathrm{d}^3 \boldsymbol{x}' W(|\boldsymbol{x}'|, h_{\mathrm{si}}) W(|\delta \boldsymbol{x}_{ji} + \boldsymbol{x}'|, h_{\mathrm{si}}). \qquad (4)$$

The probability that such an interaction occurs in a time step δt is

$$P(i|j) = \Gamma(i|j)\, \delta t, \qquad (5)$$

---

[1] This equation applies only if h_{si} is the same for both particles. See Appendix A for the general form.

and the total probability of interaction between *N*-body particles *i* and *j* is

$$P_{ij} = \frac{P(i|j) + P(j|i)}{2}. \tag{6}$$

Specifically, P_{ij} is the probability for a macroparticle representing a patch of phase space around $(\boldsymbol{x}_j, \boldsymbol{v}_j)$ to interact with a target particle representing a patch of phase space around $(\boldsymbol{x}_i, \boldsymbol{v}_i)$ in a time δt.

We determine if particles interact by drawing a random number for each pair of particles that are close enough for the probability of interaction to be greater than zero. If a pair does scatter, we do a Monte Carlo for the new velocity directions, populating these parts of the phase space and deleting the two particles at their initial phase-space locations. Note that by virtue of populating the new phase-space regions, we are taking care of the 'scattering in' term of the collision integral in equation (A1). We avoid double counting by only accounting for $P_{ij} = P_{ji}$ once during a given time step δt. In the limit of a large number of macroparticles, the total interaction probability for each particle *i* should approach

$$P_i = \sum_j P_{ij}. \tag{7}$$

We show in Section 3 that this approach correctly reproduces the expected number of scatterings in an idealized test case.

Our method for simulating scattering differs from previous approaches in a few key ways. It is most similar to that of Davé et al. (2001) in that we both directly consider interactions between pairs of phase-space patches and rely on a scattering rate similar in form to equation (3). The difference is that their geometric factor g_{ji} is not the same – our factor arises explicitly from the overlap in patches of phase space between neighbouring macroparticles, as derived from the collision term in the Boltzmann equation (see Appendix A for details). Other authors determine the scattering rate Γ of individual phase-space patches based on estimates of the local mass density (typically using some number of nearest neighbours or using a smoothed particle hydrodynamics kernel). The Monte Carlo is then based on an estimated scattering rate of an individual particle on the background, and a scattering partner is only chosen after a scattering event is determined to have occurred (Kochanek et al. 2000; Yoshida et al. 2000; Colín et al. 2002; Randall et al. 2008). The scattering probability in this latter approach is not symmetric. For macroparticles of identical mass, $P(i|j) = P(j|i)$ explicitly in our approach, but not the other approach because the density estimated at the position of macroparticle *i* need not be the same as that estimated at the position of particle *j*. In the future, there should be a direct comparison among these scattering algorithms to determine if they yield consistent results.

We have implemented our algorithm in the publicly available version of the cosmological simulation code GADGET2 (Springel 2005). GADGET2 computes the short-range gravitational interactions by means of a hierarchical multipole expansion, also known as a tree algorithm. Particles are grouped hierarchically by a repeated subdivision of space, so their gravitational contribution can be accounted by means of a single multipole force computation. A cubical root node encompasses the full mass distribution. The node is repeatedly subdivided into eight daughter nodes of half the side length each (an octree) until one ends up with 'leaf' nodes containing single particles. Forces for a given particle are then obtained by 'walking' the tree, opening nodes that are too close for their multipole expansion to be a correct approximation to their gravitational contribution. In GADGET2, spurious strong close encounters by particles are avoided

by convolving the single-point particle density distribution with a normalized spline kernel ('gravitational softening').

To implement our algorithm, we take advantage of the tree-walk already build in GADGET2, computing self-interactions during the calculation of the gravitational interactions. For this to work we have to modify the opening criterion such that nodes are opened if they are able to have particles closer than $2h_{si}$ from a target scatterer (or $h_i + h_j$ if particles have different self-interaction smoothing lengths). When computing the probability of interaction we use the same spline kernel used in GADGET2 (Monaghan & Lattanzio 1985), defined as

$$W(r, h) = \frac{8}{\pi h^3} \begin{cases} 1 - 6\left(\frac{r}{h}\right)^2 + 6\left(\frac{r}{h}\right)^3, & 0 \leq \frac{r}{h} \leq \frac{1}{2}, \\ 2\left(1 - \frac{r}{h}\right)^3, & \frac{1}{2} < \frac{r}{h} \leq 1, \\ 0, & \frac{r}{h} > 1. \end{cases} \tag{8}$$

If a pair interacts we give both particles a kick consistent with an elastic scattering that is isotropic in the centre-of-mass frame. The post-scatter particle velocities are

$$\boldsymbol{v}'_0 = \boldsymbol{v}_c + \frac{m_1}{m_0 + m_1} V\boldsymbol{e},$$
$$\boldsymbol{v}'_1 = \boldsymbol{v}_c - \frac{m_0}{m_0 + m_1} V\boldsymbol{e}, \tag{9}$$

where $\boldsymbol{v}_c$ is the centre-of-mass velocity, V is the relative speed of the particles (conserved for elastic collisions) and $\boldsymbol{e}$ is a randomly chosen direction.

The time-step criterion is also modified to assure that the scattering probability for any pair of particles is small, $P = \Gamma \delta t \ll 1$. An individual particle time step is decreased by a factor of 2 if during the last tree-walk the maximum probability of interaction for any pair involving such a particle was $P_{max} > 0.2$. Once a particle time step is modified due to the previous restriction, if $P_{max} < 0.1$ for such a particle and its current time step is smaller than the one given by the standard criterion on GADGET2, we increase it by a factor of 2.

3 TEST OF THE SIDM IMPLEMENTATION

Before performing cosmological simulations, we carried out a controlled test of the implementation in order to make sure the scattering rate and kinematics are correctly followed in the code, and to determine the optimum value of the SIDM softening kernel length h_{si}. The simplest and cleanest scenario for testing our implementation consists of a uniform sphere of particles moving through a uniform field of stationary background particles. The coordinate system is defined such as the sphere is moving along the positive *z*-direction with constant velocity v_s. The particles forming the sphere and those forming the background field are tagged as different types within the code and here we will refer to them simply as *sphere* (s) and *background* (bg) particles, respectively. We only allow scatterings involving two different types of particles (i.e. sphere–background interactions only) and turn off gravitational forces among all of the particles. Furthermore, all particles have the same mass m_p.

The expected number of interactions for this case is given by

$$N_{exp}(t) = \sum_{i \in s, j \in bg} P_{ij} = N_s(\sigma/m)\rho_{bg} v_s t, \tag{10}$$

where N_s is the total number of sphere particles, ρ_{bg} is the density of the background field and *t* is the elapsed time from the beginning of the simulation. From this experiment we have found that the number of interactions computed by the code depends on the
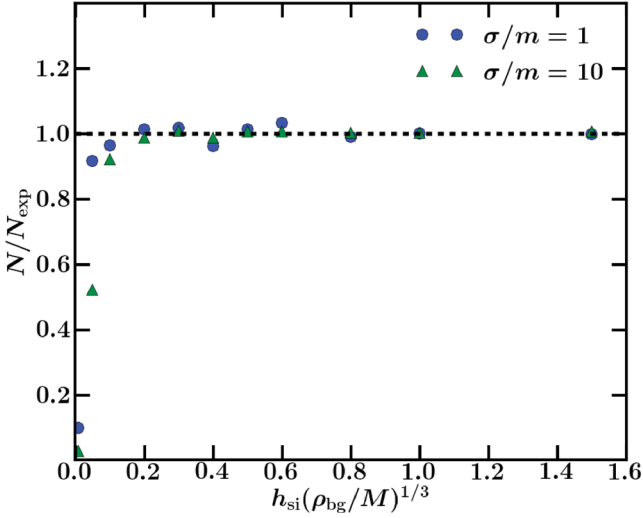
Figure 1. Fraction of the expected total number of interactions that are computed in our test simulation as a function of the self-interaction smoothing length. The self-interaction cross-section for each run is shown in units of $\mathrm{cm^2\,g^{-1}}$ in the artwork. The code converges to the expected number of interactions when the smoothing length approaches the background interparticle separation, i.e. when $h_{\mathrm{si}}(\rho_{\mathrm{bg}}/m_{\mathrm{p}})^{1/3} \gtrsim 0.2$.

self-interaction smoothing length h_{si} (see Fig. 1), which is fixed to be the same for all particles in this test. The number of interactions converges to the expected value given by equation (10) as h_{si} becomes comparable to the background interparticle separation, specifically when $h_{\mathrm{si}}(\rho_{\mathrm{bg}}/m_{\mathrm{p}})^{1/3} \gtrsim 0.2$. For $h_{\mathrm{si}}(\rho_{\mathrm{bg}}/m_{\mathrm{p}})^{1/3} \gtrsim 0.5$ the accuracy of the algorithm does not improve by much and the time of the calculations increases rapidly, $\propto h_{\mathrm{si}}^3$. Apart from the expense, using larger values of h_{si} would lead to increasingly non-local interactions among particles, which is inconsistent with the model under consideration.

We also check the kinematics of the scatters in this test simulation and describe the results in Appendix B. The resulting kinematics and number of interactions from our test simulation agree well with the expectations from the theory as long as $h_{\mathrm{si}}(\rho_{\mathrm{bg}}/m_{\mathrm{p}})^{1/3} \gtrsim 0.2$.

4 OVERVIEW OF COSMOLOGICAL SIMULATIONS

We initialize our cosmological simulations using the Multi-Scale Initial Conditions (MUSIC) code of Hahn & Abel (2011). We have a total of four initial condition sets, each run with both CDM and SIDM. The first two are cubic volumes of 25 and $50\,h^{-1}$ Mpc on a side, each with 512^3 particles. As discussed below, these simulations allow us to resolve the structure of a statistical sample of group ($\sim 10^{13}\,\mathrm{M_\odot}$) and cluster ($\sim 10^{14}\,\mathrm{M_\odot}$) haloes.

The second two initial conditions concentrate computational power on zoom regions (Katz & White 1993) drawn from the $50\,h^{-1}$ Mpc box, specifically aimed at exploring the density structure of two smaller haloes, one with virial mass[2] $M_{\mathrm{vir}} = 7.1 \times 10^{11}\,h^{-1}\,\mathrm{M_\odot} = 1 \times 10^{12}\,\mathrm{M_\odot}$ (Z12) and one with $M_{\mathrm{vir}} = 3.5 \times 10^{11}\,h^{-1}\,\mathrm{M_\odot} = 5 \times 10^{11}\,\mathrm{M_\odot}$ (Z11). The Z12 run in particular is fairly high resolution, with more than five million particles in the

---

[2] We define M_{vir} as $M_{\mathrm{vir}} = \frac{4}{3}\pi\rho_{\mathrm{b}}\Delta_{\mathrm{vir}}(z)r_{\mathrm{vir}}^3$ and r_{vir} as $\tilde{\rho}(r_{\mathrm{vir}}) = \Delta_{\mathrm{vir}}(z)\rho_{\mathrm{b}}$, where $\tilde{\rho}(r_{\mathrm{vir}})$ denotes the overdensity within r_{vir}, ρ_{b} is the background density and Δ_{vir} is the virial overdensity.

virial radius. Table 1 summarizes the simulation parameters. The cosmology used is based on 7-year *Wilkinson Microwave Anisotropy Probe* results for a ΛCDM universe: $h = 0.71$, $\Omega_{\mathrm{m}} = 0.266$, $\Omega_{\Lambda} = 0.734$, $\Omega_{\mathrm{b}} = 0.0449$, $n_{\mathrm{s}} = 0.963$ and $\sigma_8 = 0.801$ (Komatsu et al. 2011).

Each of our four initial conditions has been evolved from redshift $z = 250$ to 0 with collisionless dark matter (labelled CDM) and with two types of SIDM: one with $\sigma/m = 1\,\mathrm{cm^2\,g^{-1}}$ (labelled SIDM$_1$) and another with $\sigma/m = 0.1\,\mathrm{cm^2\,g^{-1}}$ (labelled SIDM$_{0.1}$). We can use the same initial conditions for CDM and SIDM because at high redshift the low relative velocities of the dark matter make self-interactions insignificant. Table 1 lists all the simulations used for this study and details their force, mass and self-interaction resolution. In addition to the simulations listed in Table 1, we also ran the cosmological boxes with SIDM cross-sections $\sigma/m = 0.03\,\mathrm{cm^2\,g^{-1}}$. We do not present results from these low cross-section runs here because no core density differences were resolved within the numerical convergence radii of our simulations.

As shown in Section 3, the self-interaction smoothing length h_{si} must be larger than 20 per cent of the interparticle separation in order to achieve convergence on the interaction rate. All the work for this paper was done with a fixed h_{si} for all particles carefully chosen for each simulation so that the self-interactions are well resolved at densities a few times to an order of magnitude lower than the lowest densities for which self-interactions are significant. We have run the cosmological boxes with different choices for h_{si} (changes by factors of 2–4) and have found that our results are unaffected. We have also run tests on isolated haloes with varying smoothing lengths and again find that the effects of self-interactions are robust to reasonable changes in h_{si}.

All of our halo catalogues and density profiles are derived using the publicly available code Amiga Halo Finder (AHF; Knollmann & Knebe 2009).

5 SIMULATION RESULTS

5.1 Preliminary illustrations

Before presenting any quantitative comparisons between our CDM and SIDM runs, we provide some simulation renderings in order to help communicate the qualitative differences.

The upper panels of Fig. 2 show a large-scale comparison: two ($50 \times 50 \times 10$) h^{-1} Mpc slices from the CDM-50 and SIDM$_1$-50 boxes side-by-side at $z = 0$. The structures are colour-coded by local phase-space density ($\propto \rho/v_{\mathrm{rms}}^3$). It is evident that there are no observable differences in the large-scale characteristics of CDM and SIDM$_1$. We discuss this result in more quantitative terms in Section 5.2 but of course this is expected. The SIDM models we explore do not have appreciable rates of interaction for densities outside the cores of dark-matter haloes. The upper panels of Fig. 2 provide a visual reminder that the SIDM models we consider are effectively identical to CDM on large scales.

The differences between CDM and SIDM become apparent only when one considers the internal structure of individual haloes. The lower panels of Fig. 2 provide side-by-side images of a Milky Way mass halo (Z12) simulated with CDM (left) and SIDM$_1$ (right). SIDM tends to make the cores of haloes less dense *and* kinetically hotter (see Section 5.3) and these two differences are enhanced multiplicatively in the phase-space density renderings. The central regions of the host halo are also slightly rounder in the SIDM case (Peter et al. 2012). Importantly, the difference in substructure

Table 1. Simulations discussed in this paper.

Name	Volume L_{Box} (h^{-1} Mpc)	Number of particles N_{p}	Particle mass m_{p} ($h^{-1}\,\mathrm{M_\odot}$)	Force softening ϵ (h^{-1} kpc)	Smoothing length h_{si} (h^{-1} kpc)	Cross-section σ/m ($\mathrm{cm^2\,g^{-1}}$)
CDM-50	50	512^3	6.88×10^7	1.0	–	0
CDM-25	25	512^3	8.59×10^6	0.4	–	0
CDM-Z11	$(3R_{\mathrm{vir}})^a$	2.5×10^{6a}	1.07×10^{6a}	0.3	–	0
CDM-Z12	$(3R_{\mathrm{vir}})^a$	5.6×10^{7a}	1.34×10^{5a}	0.1	–	0
$\mathrm{SIDM_{0.1}}$-50	50	512^3	6.88×10^7	1.0	2.8ϵ	0.1
$\mathrm{SIDM_{0.1}}$-25	25	512^3	8.59×10^6	0.4	2.8ϵ	0.1
$\mathrm{SIDM_{0.1}}$-Z11	$(3R_{\mathrm{vir}})^a$	2.5×10^{6a}	1.07×10^{6a}	0.3	2.8ϵ	0.1
$\mathrm{SIDM_{0.1}}$-Z12	$(3R_{\mathrm{vir}})^a$	5.6×10^{7a}	1.34×10^{5a}	0.1	1.4ϵ	0.1
$\mathrm{SIDM_1}$-50	50	512^3	6.88×10^7	1.0	2.8ϵ	1
$\mathrm{SIDM_1}$-25	25	512^3	8.59×10^6	0.4	2.8ϵ	1
$\mathrm{SIDM_1}$-Z11	$(3R_{\mathrm{vir}})^a$	2.5×10^{6a}	1.07×10^{6a}	0.3	2.8ϵ	1
$\mathrm{SIDM_1}$-Z12	$(3R_{\mathrm{vir}})^a$	5.6×10^{7a}	1.34×10^{5a}	0.1	1.4ϵ	1

^{a}The Z11 and Z12 runs are zoom simulations with multiple particle species concentrating on haloes of mass $M_{\mathrm{vir}} = 5 \times 10^{11}$ and $1.0 \times 10^{12}\,\mathrm{M_\odot}$, respectively (no h). The volumes listed refer to the number of virial radii used to find the Lagrangian volumes associated with the zoom. The particle properties listed are for the highest resolution particles only.

characteristics is minimal, especially at larger radii. We return to a quantitative description of substructure differences in Section 5.4.

5.2 Large-scale structure and halo abundances

Fig. 3 provides a quantitative comparison of both the clustering properties (left) and halo abundance evolution (right) between our full-box CDM and $\mathrm{SIDM_1}$ simulations. The left-hand panel shows the two-point function of dark-matter particles in both cosmological runs for CDM and $\mathrm{SIDM_1}$. There are no discernible differences between SIDM and CDM over the scales plotted, though of course the different box sizes (and associated resolutions) mean that the boxes themselves only overlap for a limited range of scales. For a given set of initial conditions, however, SIDM and CDM give identical results.

The right-hand panel of Fig. 3 shows the cumulative number density of dark-matter haloes (including subhaloes) as a function of their peak circular velocity (V_{max}) for the CDM-50 (solid) and $\mathrm{SIDM_1}$-50 (dashed) simulations at various redshifts. Remarkably, this comparison shows no significant difference either – indicating that SIDM with cross-sections as large as $1\,\mathrm{cm^2\,g^{-1}}$ does not strongly affect the maximum circular velocities of individual haloes. The two panels of Fig. 3 demonstrate that for large-scale comparisons, including analyses involving field halo mass functions, SIDM and CDM yield identical results. The implication is that observations of large-scale structure are just as much a 'verification' of SIDM as they are of CDM.

5.3 Halo structure

Before presenting statistics on halo structure, we focus on six well-resolved haloes that span our full mass range $M_{\mathrm{vir}} = 5 \times 10^{11} - 2 \times 10^{14}\,\mathrm{M_\odot}$, selected from our full simulation suite, including our two zoom-simulation haloes (Z12 and Z11). Figs 4–6 show radial profiles for the density, circular velocity and velocity dispersion for all three dark matter cases. In each figure, black circles correspond to CDM, green triangles to $\mathrm{SIDM_{0.1}}$ and blue stars to $\mathrm{SIDM_1}$. All profiles are shown down to the innermost resolved radius for which the average two-body relaxation time roughly matches the age of the Universe (Power et al. 2003).

We begin with the density profiles of haloes shown in the six-panel Fig. 4. For each halo in the CDM run, we have fit an NFW profile (Navarro et al. 1997) to its radial density structure,

$$\rho_{\mathrm{NFW}}(r) = \frac{\rho_{\mathrm{s}} r_{\mathrm{s}}^3}{r(r_{\mathrm{s}} + r)^2}, \tag{11}$$

and recorded its corresponding scale radius r_{s}. The CDM-fit r_{s} value for each halo is given in its associated panel along with the halo virial mass. The radial profiles for each halo (in both the CDM and SIDM runs) are normalized with respect to the CDM r_{s} value in the plot. This allows our full range of halo masses to be plotted on identical axes.

The SIDM versions of each halo show remarkable similarity to their CDM counterparts at large radii. However, the $\mathrm{SIDM_1}$ cases clearly begin to roll towards constant-density cores at small radii. The best resolved haloes in the $\mathrm{SIDM_{0.1}}$ runs also demonstrate lower central densities compared to CDM, though the differences are at a factor of $\sim$2 level even in our best resolved systems. Clearly, higher resolution simulations will be required in order to fully quantify the expected differences between CDM and SIDM for $\sigma/m \sim 0.1\,\mathrm{cm^2\,g^{-1}}$.

For the $\mathrm{SIDM_1}$ cases, we can quantify the halo cores by fitting them to Burkert (1995) profiles:

$$\rho_{\mathrm{B}}(r) = \frac{\rho_{\mathrm{b}} r_{\mathrm{b}}^3}{(r + r_{\mathrm{b}})(r^2 + r_{\mathrm{b}}^2)}. \tag{12}$$

These Burkert fits are shown as blue dashed lines. They are good fits for radii within $\sim$2–3r_{s}, but the quality of the fits gets worse at large radii. The blue arrows in each panel show the value of the best-fitting Burkert core radius for the $\mathrm{SIDM_1}$ haloes. Note that the values are remarkably stable in proportion to the CDM r_{s} value at $r_{\mathrm{b}} \simeq 0.7 r_{\mathrm{s}}$.

As explained in Section 7, the fact that the $\mathrm{SIDM_1}$ profiles are reasonably well characterized by a single scale-radius Burkert profile may be a lucky accident, only valid for cross-sections near $1\,\mathrm{cm^2\,g^{-1}}$. It just so happens that for this cross-section the radius where dark-matter particles experience significant scattering sets in at $r \sim r_{\mathrm{s}}$ (see Fig. 7 and related discussion). For a smaller cross-section (with a correspondingly smaller core) a multiple parameter fit may be necessary. Given the beginnings of very small cores we
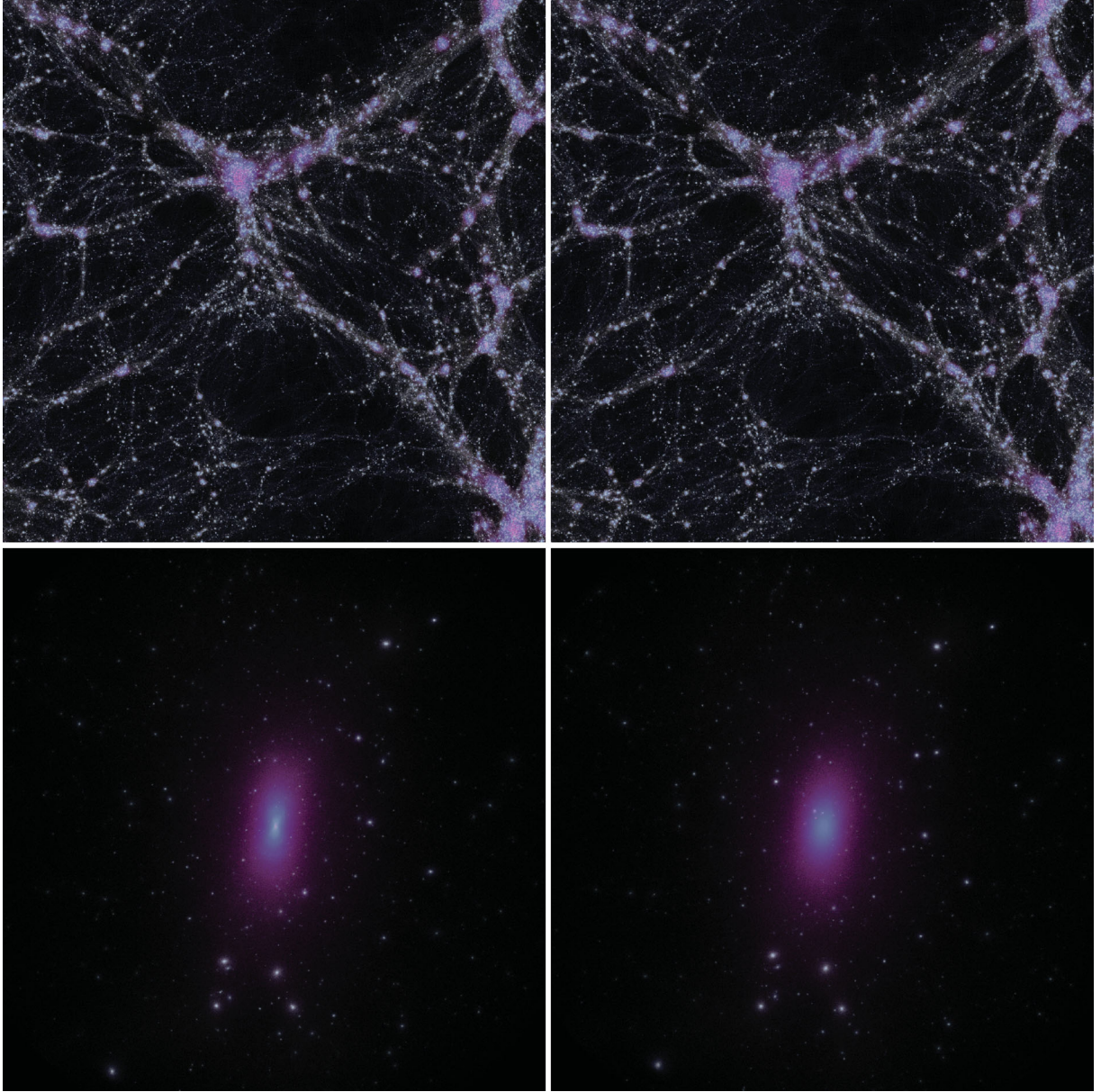
Figure 2. Top: large-scale structure in CDM (left) and $SIDM_1$ (right) shown as a 50×50 h^{-1} Mpc slice with 10 h^{-1} Mpc thickness through our cosmological simulations. Particles are coloured according to their local phase-space density (white densest). There are no visible differences between the two cases. Bottom: small-scale structure in a Milky Way mass halo (Z12) simulated with CDM (left) and $SIDM_1$ (right), including all particles within $200\,h^{-1}$ kpc of the halo centres. The magnitude of the central phase-space density is lower in SIDM because the physical density is lower *and* the velocity dispersion is higher. The core of the SIDM halo is also slightly rounder. Note that substructure content is quite similar except in the central regions.

are seeing in the $SIDM_{0.1}$ runs, it appears that we would need one scale radius to define an r_s bend and a second scale radius to define a distinct core.

Another qualitative fact worth noting is that the density profiles of the $SIDM_1$ haloes overshoot the CDM density profiles near the Burkert core radius (not as much as the Burkert fits do, but the difference in the data points is noticeable). This is due to the fact that as particles scatter in the centre, those that gain energy are pushed to larger apocentre orbits. This observation invites us to consider a toy model for SIDM haloes where the effect of SIDM is confined to a region (smaller than a radius of about r_b) wherein particles redistribute energy and move towards a constant-density isothermal core. We will develop this model further to explain the scaling relations between core size and halo mass in Section 6.

The circular velocity curves for the same set of haloes discussed above are shown in Fig. 5. The SIDM rotation curves rise more steeply and have a lower normalization than for CDM within the NFW scale radius r_s. This brings to mind the rotation curves observed for low surface brightness galaxies and we will explore this connection later. Note though that the peak circular velocity V_{max} actually is slightly higher for the $SIDM_1$ case because of the mass rearrangement (evident in the density profiles in Fig. 4) briefly discussed in the last paragraph. At radii well outside the core radius, the rotation curves of the CDM and $SIDM_1$ haloes converge, though this convergence occurs beyond the plot axes $> r_s$ for most of the haloes shown.

An appreciation of why the density profiles of SIDM haloes become cored can be gained from studying their velocity dispersion
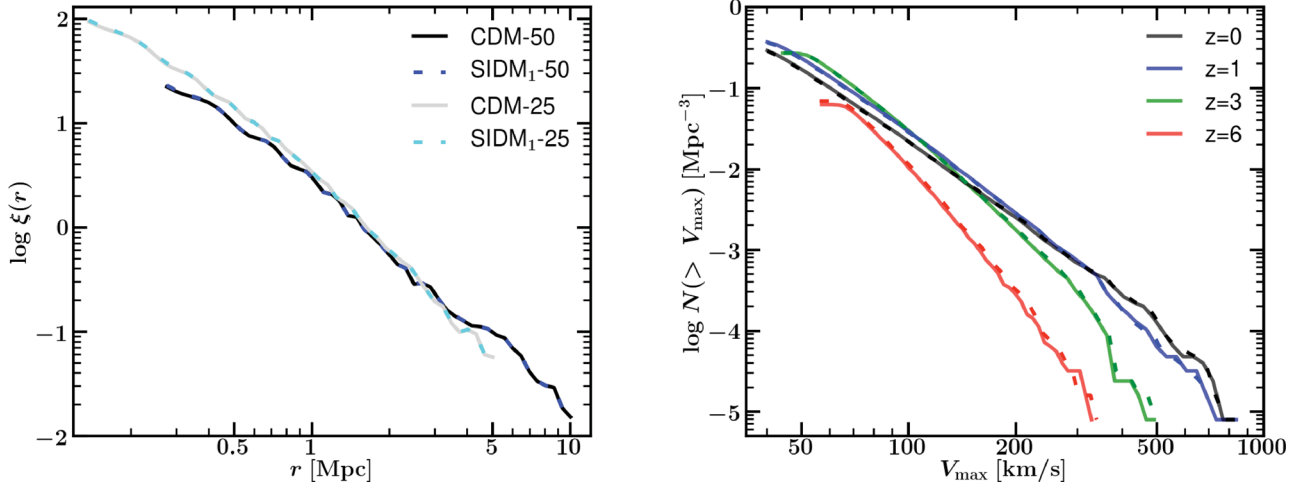
Figure 3. Large-scale characteristics. Left: dark-matter two-point correlation functions from our CDM-50 (CDM-25) and SIDM$_1$-50 (SIDM$_1$-25) simulations in black (grey) and blue (cyan) colours, respectively. There are no noticeable differences between the CDM and SIDM$_1$ dark-matter clustering over the scales plotted. Right: cumulative number density of dark-matter haloes as a function of their maximum circular velocity (V_{max}) at different redshifts for our CDM-50 (solid) and SIDM$_1$-50 (dashed) simulations. There are no significant differences in the V_{max} functions of CDM and SIDM$_1$ at any redshift.
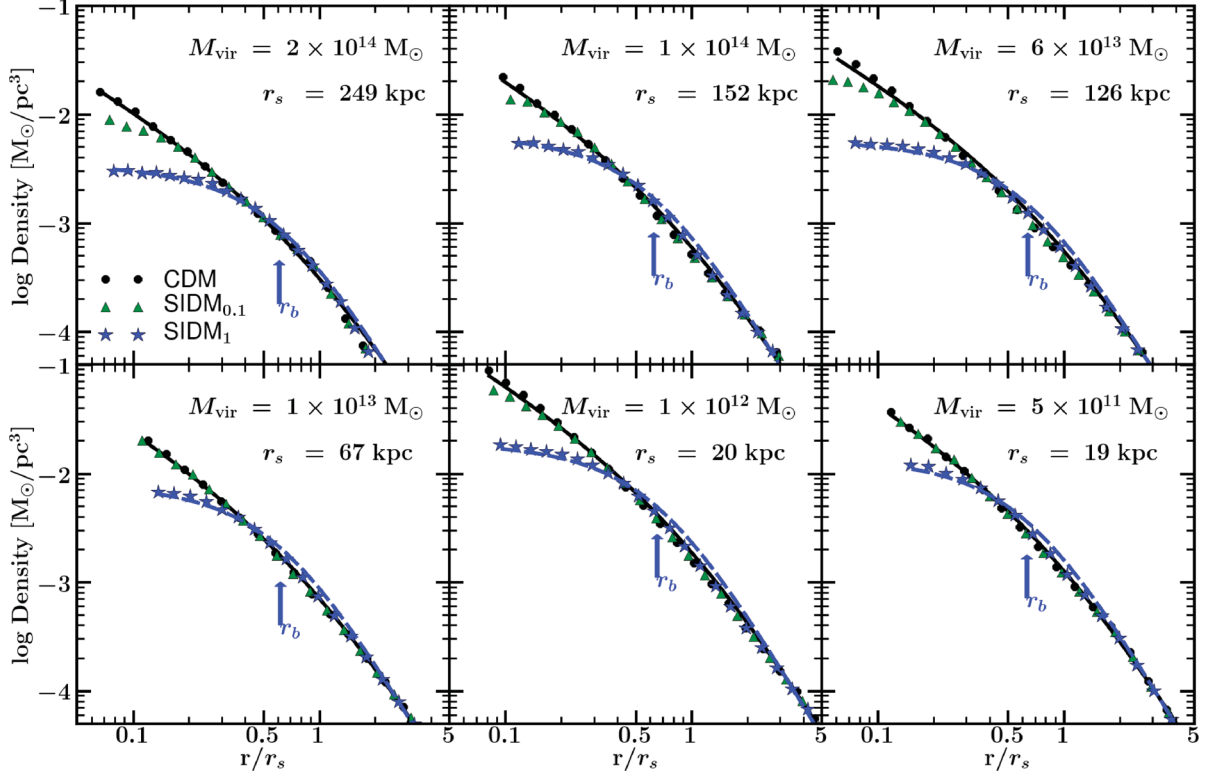
Figure 4. Density profiles for our six example haloes from our SIDM$_1$ (blue stars) and SIDM$_{0.1}$ (green triangles) simulations and their CDM counterparts. With self-interactions turned on, halo central densities decrease, forming cored density profiles. Solid lines are for the best NFW (black) and Burkert (blue) fits, with the points representing the density at each radial bin found by AHF. The arrow indicates the location of the Burkert core radius r_b. r_s is the NFW scale radius of the corresponding CDM halo density profile (black solid line). Burkert profiles provide a reasonable fit to our SIDM$_1$ haloes only because $r_b \approx r_s$ for $\sigma/m = 1\,\mathrm{cm^2\,g^{-1}}$, so a cored profile with a single scale radius works. As discussed in Section 7, this is not the case for $\sigma/m = 0.1\,\mathrm{cm^2\,g^{-1}}$ and thus Burkert profiles are not a good fit to our SIDM$_{0.1}$ haloes.

profiles compared to their CDM counterparts, as illustrated in Fig. 6. Here, v_{rms} is defined as the root mean square speed of all particles within radius r. While the CDM haloes (black) are colder in the centre than in their outer parts (reflecting a cuspy density profile) the SIDM haloes have hotter cores, indicative of heat transport from the outside in. Moreover, the SIDM haloes are slightly *colder* at large

radii, again reflecting a redistribution of energy. As discussed in the introduction, it is this heat transport that is the key to understanding why CDM haloes differ from SIDM haloes in their density structure (Balberg et al. 2002; Colín et al. 2002; Ahn & Shapiro 2005; Koda & Shapiro 2011). The added thermal pressure at small radii is what gives rise to the core. The SIDM$_1$ simulations have sufficient
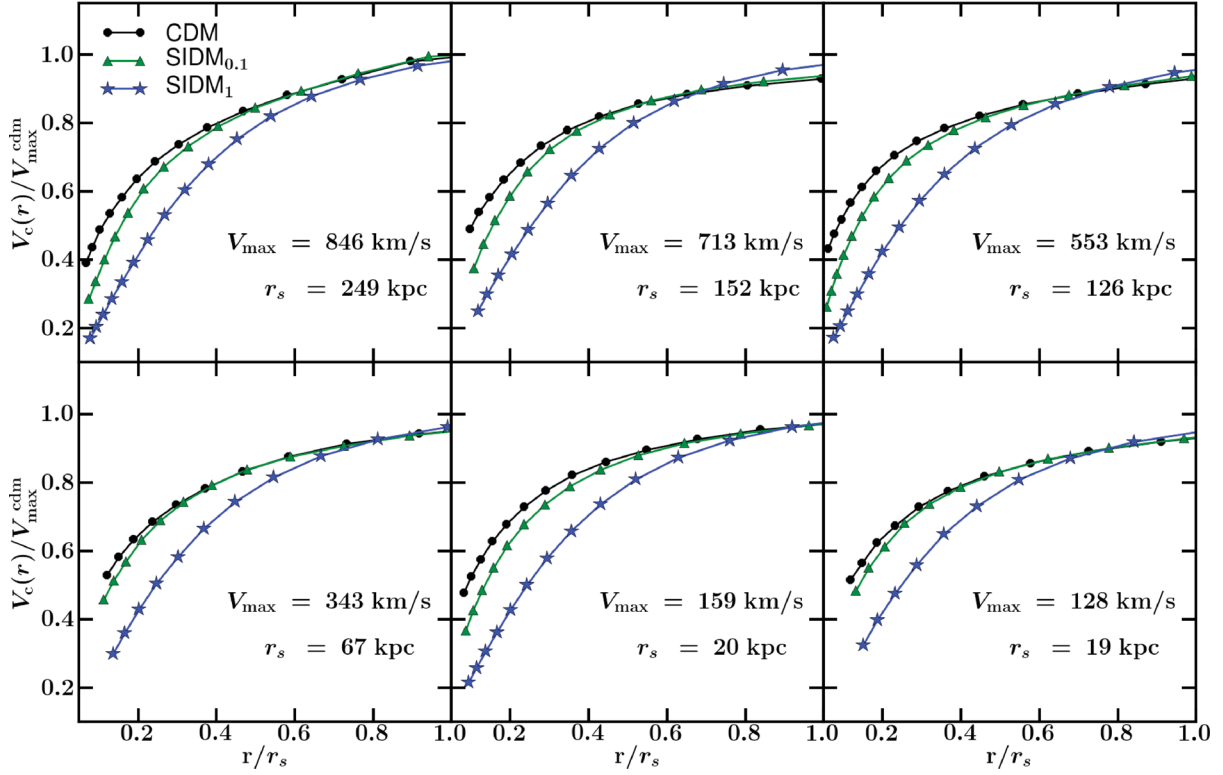
Figure 5. Circular velocity profiles for our example selection of six well-resolved haloes from our CDM, SIDM$_1$ and SIDM$_{0.1}$ simulations. The magnitude of the circular velocity at small radii ($r \lesssim r_s$) is lowered for all haloes when self-interactions are turned on. r_s is the NFW scale radius of the corresponding CDM halo density profile.
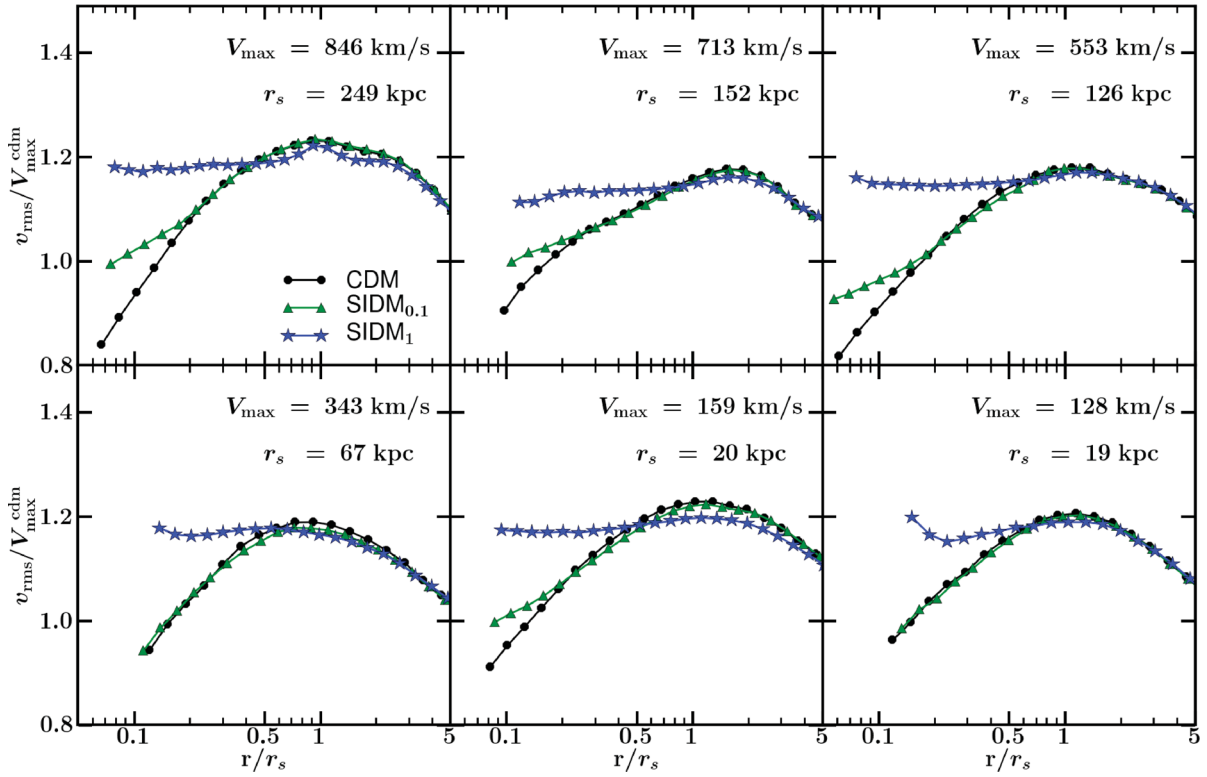

Figure 6. Velocity dispersion profiles for our six example haloes from our SIDM$_1$ and SIDM$_{0.1}$ simulations overplotted with their CDM counterparts. The velocity dispersion is inflated at small radii and slightly suppressed at large radii. The effects set in at approximately the radius where SIDM particles experience at least one interaction on average over the lifetime of the halo (see Fig. 7).
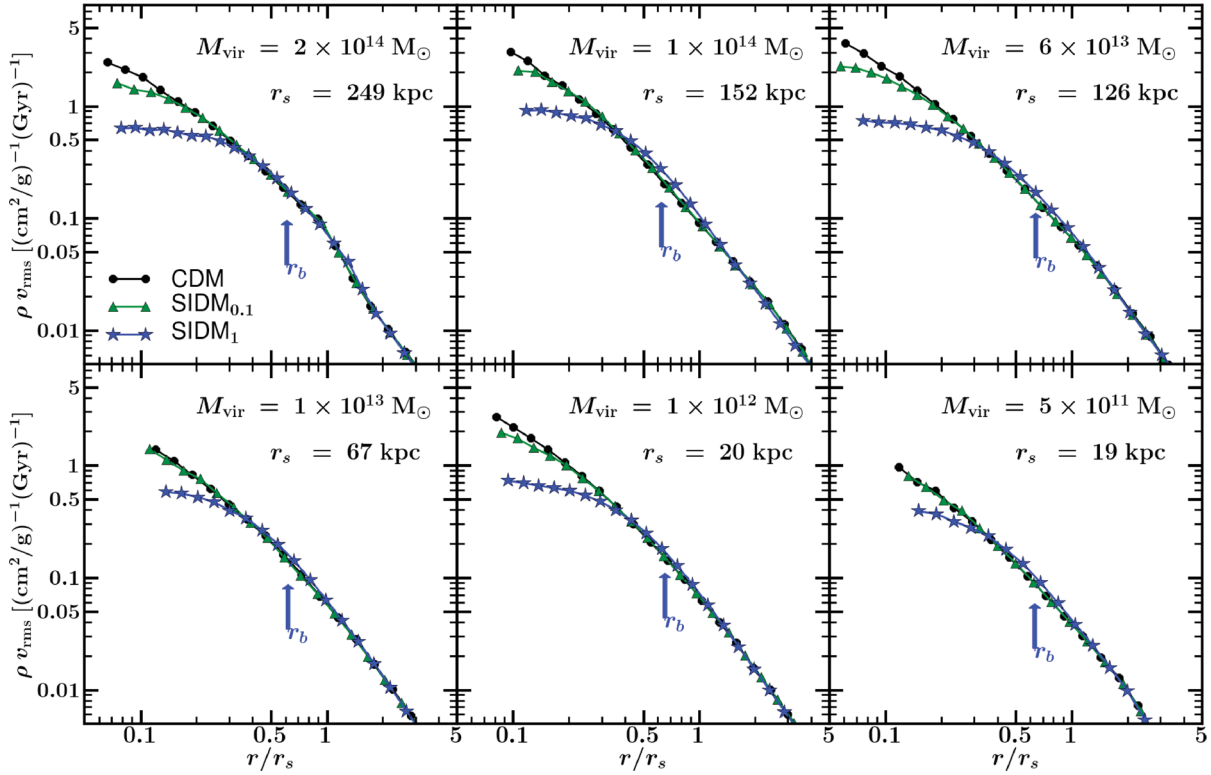
Figure 7. Estimate of the local scattering rate modulo the cross-section $\rho v_{rms} = \Gamma(\sigma/m)^{-1}$ for six well-resolved haloes from our CDM, SIDM$_{0.1}$ and SIDM$_1$ simulations. The quantity is scaled by $1\mathrm{Gyr}\,\mathrm{cm}^2\,\mathrm{g}^{-1}$, such that '1' in these units means that each particle has roughly one interaction per Gyr in SIDM$_1$ and 0.1 per Gyr in SIDM$_{0.1}$. Based on this argument, the effects of self-interactions in the properties of haloes over ~ 10 Gyr should start to become important when the ordinate is greater than about 0.1 in SIDM$_1$ ($r/r_s \sim 0.8$) and greater than about 1 in SIDM$_{0.1}$ ($r/r_s \sim 0.2$). Comparisons to Figs 4–6 indicate that this is indeed the case.

interactions that they have been driven to isothermal profiles for $r/r_s \lesssim 1$, while for SIDM$_{0.1}$ the v_{rms} profiles typically begin to deviate from the CDM lines only at smaller radii, $r/r_s \sim 0.2$, reflecting the relatively lower scattering rate.

The deviations in the SIDM v_{rms} profiles compared to CDM appear to set in at approximately the radius where we expect every particle to have interacted once in a Hubble time. This is explored directly in Fig. 7, where we present a proxy for the local scattering rate as a function of distance from the halo centre:

$$\rho(r)\, v_{rms}(r) \propto \Gamma(r)\, (\sigma/m)^{-1}. \qquad (13)$$

We have divided out the cross-section, so it is easier to compare the SIDM$_{0.1}$ and SIDM$_1$ cases. Fig. 7 presents this rate proxy in units of $1\mathrm{Gyr}\,\mathrm{cm}^2\,\mathrm{g}^{-1}$; for the SIDM$_1$ case (with $\sigma/m = 1\,\mathrm{cm}^2\,\mathrm{g}^{-1}$), the radius where a typical particle will have scattered once over a 10 Gyr halo lifetime is $\rho(r)v_{rms}(r) = 0.1$. For the SIDM$_{0.1}$ case (with $\sigma/m = 0.1\,\mathrm{cm}^2\,\mathrm{g}^{-1}$), the ordinate needs to be 10 times higher (~ 1) in order to achieve the same scattering rate.

By comparing Fig. 7 to Fig. 6 (and to some extent to all Figs 4–6), we see that the effects of self-interactions do become evident at radii corresponding to $\rho\, v_{rms} \sim 0.1$ for SIDM$_1$ (at $r/r_s \sim 0.8$) and $\rho\, v_{rms} \sim 1$ for SIDM$_{0.1}$ (at $r/r_s \sim 0.2$). Interestingly, for the SIDM$_1$ haloes this interaction radius is fairly close to the Burkert scale radius (shown by the blue arrows). It should be kept in mind, however, that the structure of haloes can be affected at larger radii because particles scattering in the inner regions can gain energy and move to larger orbits. A careful inspection of the density and rotation velocity profiles shows that this is indeed the case.

We will discuss these findings in more detail in Sections 6 and 7. In particular, in Section 7 we present an analytic model aimed at understanding how the central densities and scale radii of SIDM haloes are set in the context of energetics. Moreover, before moving on to those issues, we first explore halo substructure in SIDM.

5.4 Substructure

The question of halo substructure is an important one for SIDM. One of the original motivations for SIDM was to reduce the number of subhaloes in the Milky Way halo in order to match the relative dearth of observed satellite galaxies (Spergel & Steinhardt 2000). However, the overreduction of halo substructure is now recognized as a negative feature of SIDM compared to CDM, given the clear evidence for galaxy-size subhaloes throughout galaxy clusters (Natarajan et al. 2009) and the new discoveries of ultrafaint galaxies around the Milky Way (see Bullock 2010; Willman 2010 for reviews). In fact, one of the most stringent constraints on the self-interaction cross-section comes from analytic subhalo-evaporation arguments (Gnedin & Ostriker 2001).

Fig. 8 demonstrates that the effects of subhalo evaporation in SIDM are not as strong as previously suggested on analytic grounds. Here we show the cumulative number of subhaloes larger than a given V_{max} for a sample of well-resolved haloes in our CDM (solid), SIDM$_{0.1}$ (dotted) and SIDM$_1$ (dashed) simulations. The associated virial masses for each host halo are shown in the artwork. The left-hand panel presents the V_{max} function for all subhaloes within the virial radius of each host and the right-hand panel restricts the analysis to subhaloes within half of the virial radius. We see that
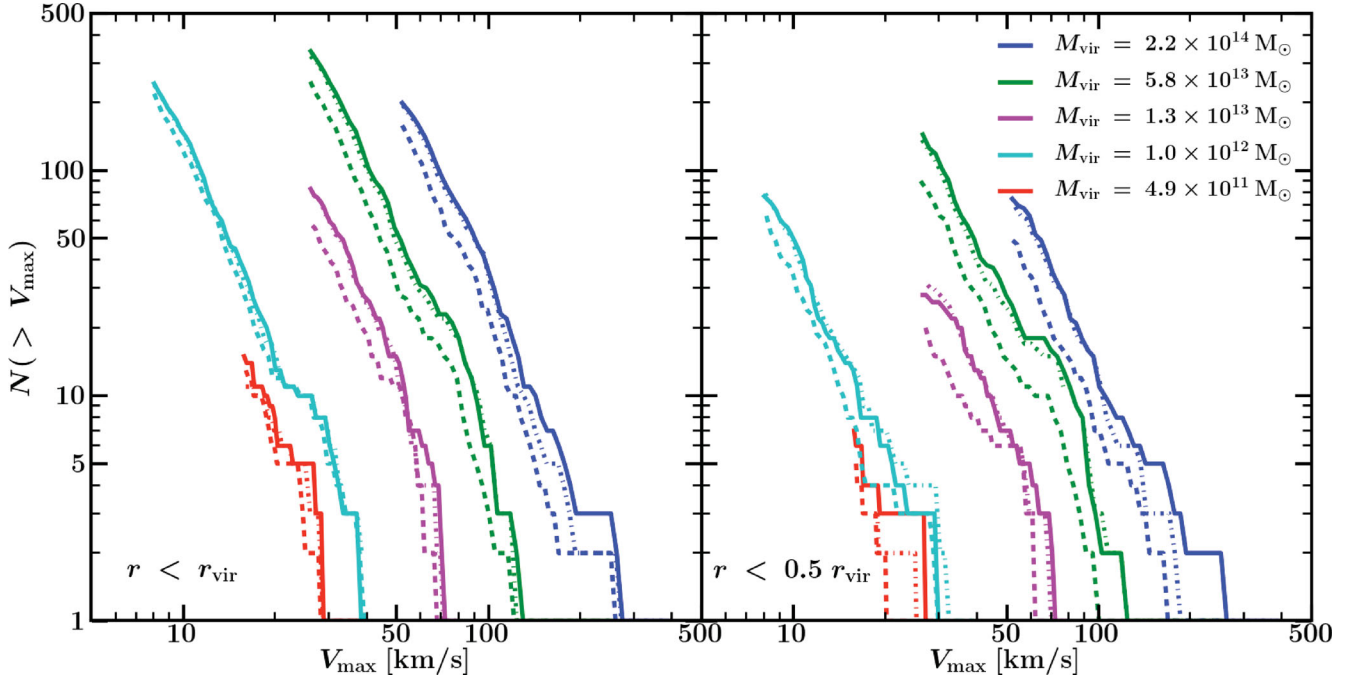
Figure 8. Subhalo cumulative number as a function of halo peak circular velocity (V_{max}) for several well-resolved haloes in our CDM (solid), SIDM$_{0.1}$ (dotted) and SIDM$_1$ (dashed) simulations. When looking at all subhaloes within $r < r_{vir}$ (left), the differences are small and the slope of the subhalo V_{max} function is the same for the CDM and SIDM cases. The offset in the subhalo V_{max} function increases when we look only at subhaloes inside $r < 0.5r_{vir}$ (right-hand panel), showing that SIDM suppresses the number of subhaloes in the central regions of haloes more strongly.

generally the reduction in substructure counts at a fixed V_{max} is small but non-zero and that the effects appear to be stronger at small radii than large. Similarly, there appears to be slightly more reduction of substructure in the SIDM cluster haloes compared to the galaxy size systems.

We can understand the following two trends: (1) the increase in the difference between the CDM and SIDM V_{max} functions as M_{vir} increases and (2) the increase in the difference as one looks at the central regions of the halo, using the results from the previous section as a guide. The typical probability that a particle in an SIDM subhalo will interact with a particle in the background halo is

$$P \approx \langle \rho_{host}(r)(\sigma/m)v_{orb}(r) \rangle_T \, T, \tag{14}$$

where $v_{orb}(r)$ is the orbital speed of the subhalo at position r, ρ_{host} is the mass density of the host halo and T is the orbital period. The typical speed of the subhalo is similar to the rms speed of the smooth component of the halo, and thus $\rho_{host}(r)(\sigma/m)v_{orb}(r)$ should be similar to the function we show in Fig. 7. At fixed r/r_s we expect P to scale with V_{max} as V_{max}^3/r_{max}^2 (given that $\rho_s \propto V_{max}^2/r_{max}^2$), which is a very mildly increasing function of V_{max} over the range of halo masses we have simulated. Note though that we expect scatter at fixed halo mass because of the scatter in the $V_{max}-r_{max}$ relation (Bullock et al. 2001).

While the increase in destruction of subhaloes with host halo mass is not strong, it is clear from the above arguments that subhaloes in the inner parts of the halo ($r/r_s \ll 1$) should be destroyed but the bulk of the subhaloes around $r/r_s \sim 1$ and beyond should survive for $\sigma/m = 1\,\mathrm{cm^2\,g^{-1}}$. This effect is strengthened by the fact that subhaloes in the innermost region of the halo were accreted much longer ago than subhaloes in the outskirts, so they have experienced many more orbits (Rocha, Peter & Bullock 2012). These arguments explain the comparisons between the subhalo mass functions plotted in Fig. 8. Our arguments demonstrate that a large fraction of the

subhaloes found in CDM haloes (most of which are in the outer parts) would still survive in SIDM haloes for σ/m values around or below $1\,\mathrm{cm^2\,g^{-1}}$.

Overall in the previous two sections we have seen that the effects of self-interactions between dark-matter particles in cosmological simulations are primarily in the central regions of dark-matter haloes, leaving the large-scale structure identical to our non-interacting CDM simulations. Thus, we retain the desirable features of CDM on large scales while revealing different phenomenology near halo centres. In the following section, we will move to explore how the properties of SIDM haloes presented here scale with halo mass.

6 SCALING RELATIONS

In the previous section we saw that while SIDM preserves the CDM large-scale properties of dark-matter haloes, self-interactions in the central regions of haloes result in a decrease of central densities and the formation of cores in their density profiles. We found that the density profiles of haloes from our SIDM$_1$ simulations can be relatively well fit by Burkert density profiles inside $r \sim 2-3r_s$ (see Fig. 4). Here we define a sample of well-resolved haloes from all our SIDM$_1$ simulations and use Burkert fits to their density profiles in order to quantify their central densities and core sizes. We then provide scaling relations of dark-matter halo properties with maximum circular velocity V_{max}.

The sample of haloes used for the rest of this section consists of the two host haloes in our SIDM$_1$-Z11 and SIDM$_1$-Z12 simulations together with the 25 most massive haloes from our SIDM$_1$-50 and the 25 most massive haloes from our SIDM$_1$-25 simulations. That gives us a total of 52 haloes spanning a range $V_{max} = 30-860\,\mathrm{km\,s^{-1}}$ or $M_{vir} = 5 \times 10^{11}-2 \times 10^{14}\,\mathrm{M_\odot}$. For this set of haloes the innermost resolved radius, defined by equation

(20) in Power et al. (2003), is always smaller than one-third of the Burkert scale radius from which we define the sizes of cores. It is vital that we do a conservative comparison to the Power et al. (2003) radius because both gravitational scattering and self-interactions lead to the same phenomenological result of constant-density cores. Most of the haloes (other than the 52 we select here) do not pass this test well enough for the core set by self-interactions to be resolved with confidence. This desire to be conservative in our presentation of scaling relations forces us to find these relations from only a small sample of haloes for $SIDM_1$ and leaves us with basically no haloes to find scalings for $SIDM_{0.1}$. Moreover, one has to keep in mind that our $SIDM_1$ relations could be biased by selecting only the most massive haloes in our full-box simulations. Evidently higher resolution simulations are necessary to find definitive answers. It is reassuring however that the scaling relations derived from our analytical arguments in Section 7 agree so well with the ones presented here for $\sigma/m = 0.1 \, \mathrm{cm^2 \, g^{-1}}$.

We have checked that for all of our haloes we resolve the scattering rate out to at least four times the Burkert scale radius. Outside of this point the scattering rate is underestimated because of our choice of the self-interaction smoothing length relative to the interparticle spacing (see Section 3). However, the expected scattering rate is negligible with respect to the Hubble rate outside that radius (Fig. 7). Moreover, we have re-run our $50 \, h^{-1}$ Mpc boxes for a range of SIDM smoothing values and found identical results. Thus, we consider our sample to be well resolved.

Eight haloes in our sample are undergoing significant interactions and have density profiles that are clearly perturbed even in the CDM runs. We include these eight systems in all of the following plots but indicate them with open symbols. We do not use them in the best fits for the scaling relations that we provide.

We start by examining the global structure of haloes as characterized by the maximum circular velocity V_{max} and the radius where the rotation curve peaks, r_{max}. The relationship between V_{max} and r_{max} provides a simple, intermediate-scale measure of halo concentration and we aim to investigate any differences between SIDM and CDM. Fig. 9 shows the $V_{max}-r_{max}$ relation for CDM (black) and $SIDM_1$ (blue) haloes. We can see that small differences of about

Figure 10. Burkert scale radius versus V_{max} for our combined sample of well-resolved haloes from our $SIDM_1$-50 (blue circles), $SIDM_1$-25 (green stars), $SIDM_1$-Z12 (cyan square) and $SIDM_1$-Z11 (red triangle) simulations. Open symbols correspond to haloes that are undergoing mergers. These perturbed haloes were not included in the fit for the scaling relation. A single power law holds along the whole range of our sample, suggesting that this dependence continues towards smaller and larger V_{max} values.

10 per cent exist in both V_{max} and r_{max}, with $SIDM_1$ haloes having larger values for V_{max} and smaller for r_{max}. This was already evident in Fig. 5, where the circular velocity curves of $SIDM_1$ haloes seem to peak at slightly smaller radii and slightly larger velocities than their CDM analogues, even though $SIDM_1$ curves decrease more steeply at the centre.

The apparent difference is consistent with a picture where energy exchange due to scattering redistributes the SIDM dark-matter particles, with many of the tightly bound particles scattered on to less bound, high-apocentre orbits. Since the radius at which self-interactions are significant (see Fig. 7) is smaller than (but close to) r_s, it is entirely reasonable that the scattered particles lead to a new r_{max} for $SIDM_1$ that is smaller than the CDM r_{max} and a V_{max} that is larger. Note that the slope of the $V_{max}-r_{max}$ relation is unchanged from CDM to $SIDM_1$. The best-fitting relations are

$$r_{max} = 26.21 \, \mathrm{kpc} \left(\frac{V_{max}}{100 \, \mathrm{km \, s^{-1}}} \right)^{1.45} \quad (\mathrm{CDM}) \, ,$$

$$r_{max} = 22.46 \, \mathrm{kpc} \left(\frac{V_{max}}{100 \, \mathrm{km \, s^{-1}}} \right)^{1.46} \quad (\mathrm{SIDM_1}). \quad (15)$$

We continue this discussion by considering the sizes of cores in our $SIDM_1$ simulations as a function of V_{max}. The core sizes of haloes are quantified by the scale radius in the Burkert fit to their density profiles, namely r_b in equation (12). Fig. 10 shows that for this relation a single power law holds along the whole range of our sample. We will come back to this result in Section 8 on extrapolating to smaller and larger V_{max} values to make contact with observations of cores in galaxies and clusters. The power law that best fits our data is given by

$$r_b = 7.50 \, \mathrm{kpc} \left(\frac{V_{max}}{100 \, \mathrm{km \, s^{-1}}} \right)^{1.31}. \quad (16)$$

If we fit to M_{vir} instead of V_{max}, we get

$$r_b = 2.21 \, \mathrm{kpc} \left(\frac{M_{vir}}{10^{10} \, \mathrm{M_\odot}} \right)^{0.43}. \quad (17)$$
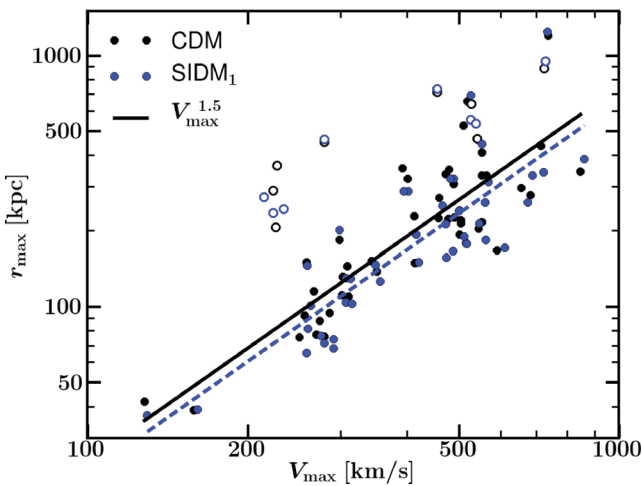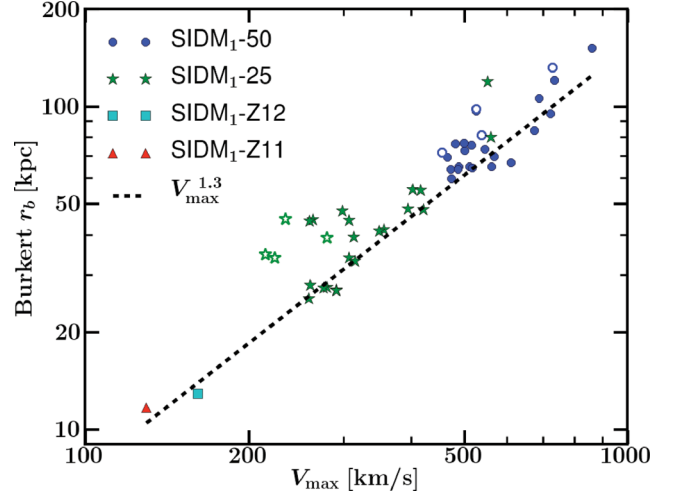

Figure 9. r_{max} versus V_{max} for our combined sample of well-resolved haloes from our $SIDM_1$ and CDM simulations. Open symbols correspond to haloes for which the density profiles showed signs of being perturbed, thus they were not included in the best fit of the relation. Small differences of about 10 per cent exists in both V_{max} and r_{max}; however, the slope of $V_{max}-r_{max}$ relation is unchanged from CDM to $SIDM_1$.
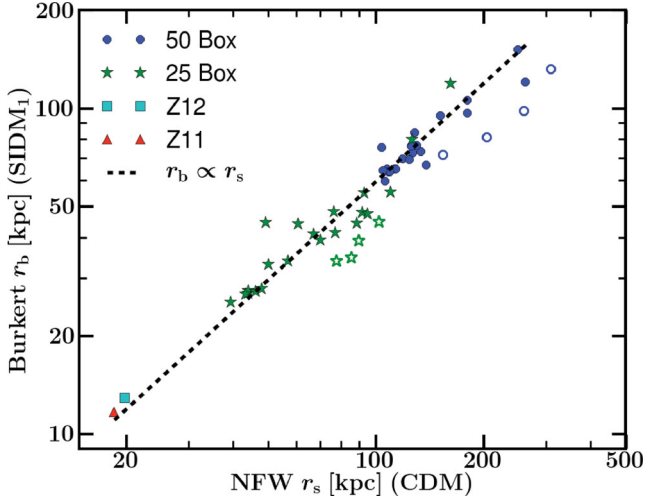
Figure 11. Burkert scale radius in SIDM$_1$ haloes versus the NFW scale radius in their CDM counterparts. Points and labels are the same as in Fig. 10. There is a one-to-one correlation indicating that the core size of SIDM$_1$ haloes scales the same as the scale radius of CDM haloes with V_{max}.

We note that the scaling with V_{max} is close to that expected for r_{max} or r_s. We show this explicitly by fitting for the core size of SIDM$_1$ haloes r_b as a function of the NFW scale radius r_s of their CDM counterparts, as shown in Fig. 11. We find that the ratio of the core size of an SIDM$_1$ halo to the scale radius of the corresponding CDM halo varies very mildly with V_{max}. In other words, the core sizes are a fixed fraction of the CDM halo scale radius. The relation that best fits our data is given by

$$\frac{r_b}{r_s} = 0.71 \left(\frac{r_s}{10\,\mathrm{kpc}} \right)^{-0.08}. \tag{18}$$

This underscores the point that r_b and r_s are closely tied to each other and the fact that they are numerically so close to each other is the reason why a cored profile with a single scale (like a Burkert profile) provides a reasonable fit to our SIDM$_1$ haloes. We will explain this striking behaviour using an analytic model in the next section.

The central densities in SIDM$_1$ haloes can be defined either as the Burkert profiles scale density or as the density at the innermost resolved radius. We have found that both definitions give similar results with no significant differences. In Fig. 12, we show how the Burkert scale density ρ_b scales with V_{max}. The trend in the $\rho_b - V_{max}$ relation is not as strong as for the $r_b - V_{max}$ relation, with a scatter as large as about a factor of 3. We will come back to the implications of this result in Section 8. The relation that best fits our data is given by

$$\rho_b = 0.015\,\mathrm{M_\odot\,pc^{-3}} \left(\frac{V_{max}}{100\,\mathrm{km\,s^{-1}}} \right)^{-0.55}. \tag{19}$$

If we fit to M_{vir} instead of V_{max}, we get

$$\rho_b = 0.029\,\mathrm{M_\odot\,pc^{-3}} \left(\frac{M_{vir}}{10^{10}\,\mathrm{M_\odot}} \right)^{-0.19}. \tag{20}$$

We urge caution when using the above fits to the central densities as it is likely to be affected by our small sample size given the large scatter. The toy model discussed in the next section predicts a slightly stronger scaling with V_{max}. However, the typical densities of the order of 0.01 M$_\odot$ pc^{-3} for galaxy haloes and 0.001 M$_\odot$ pc^{-3}
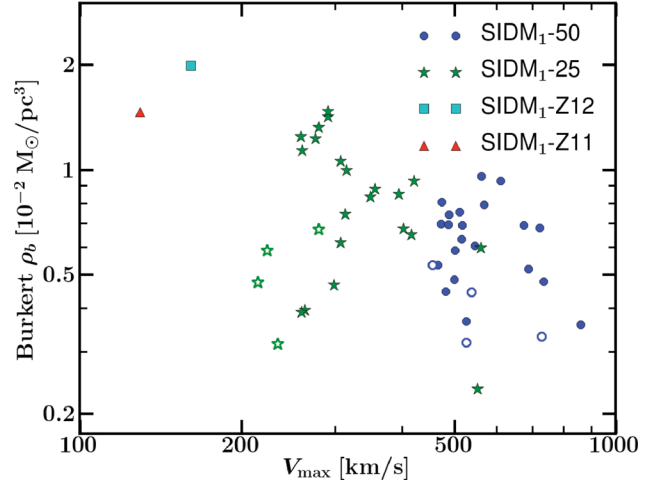

Figure 12. Burkert scale density versus V_{max}. Points and labels are the same as in Fig. 10. The trend in the $\rho_b - V_{max}$ relation is not as clear as for the $r_b - V_{max}$ relation, with a scatter of up to a factor of 3.

for cluster haloes (see Fig. 12) are in line with the predictions of the analytic model.

In this section, we have presented scaling relations for the properties of haloes in our SIDM$_1$ simulations. Our limited resolution allows us to use only 52 haloes spanning a modest mass range, from which we throw out eight systems that are undergoing mergers. Admittedly, this sample is not large enough to be definitive, especially in regards to scatter. However, the strong correlation between the SIDM core radius r_b and the counterpart CDM scale radius r_s is clearly statistically significant and the general trends provide a useful guide for tentative observational comparisons – a subject we will return to in the final section below.

7 ANALYTIC MODEL TO EXPLAIN THE SCALING RELATIONS

In this section, we develop a simple model to understand the scaling relations shown in Section 6. This model is based on identifying an appropriate radius r_1 within which self-interactions are effective and demanding that the mass as well as the average velocity dispersion within this radius are set by the mass and the average velocity dispersion (within the same radius) of the *same halo in the absence of self-scatterings*. The mass loss due to scatterings in the core should be insignificant because particles rarely get enough energy to escape and this implies that the mass within r_1 should be close to what it would have been in the absence of self-interactions. This also implies that the potential outside r_1 is unchanged from its CDM model prediction, but tends to a constant value faster inside r_1. Within this set of approximations, the dominant effect due to scatterings is to redistribute kinetic energy in the core, while keeping the total kinetic energy within r_1 the same as it would have had before self-interactions became important. We have looked at the kinetic energy profiles in the best-resolved haloes in our simulations and have confirmed that this is indeed a good approximation. Note that in this picture, there is a clear demarcation of time-scales such that the inner halo structure (say $r \lesssim r_s$) is set (the same way as in the CDM model) well before self-interactions become important. For cross-sections much larger than what we are interested in here, this need not hold.

To set up the model, we start by recalling that self-interactions work to create an isothermal core (see Fig. 6) that is isotropic (both

spatially and in velocity space). Using the spherical Jeans equation, one can then see that for a system with these properties

$$v_{\text{rms},0}^2 = 3\sigma_{\text{r}}(0)^2 = 2\pi\xi^{-1} G\rho(0)r_0^2 \,, \tag{21}$$

where we have defined r_0 to be the expansion parameter such that $\rho(r)\sigma_{\text{r}}(r)^2 = \rho(0)\sigma_{\text{r}}(0)^2[1 - \xi(r/r_0)^2]$ when $r \ll r_0$ and σ_{r} is the radial velocity dispersion. The form of the Taylor expansion for $\rho(r)\sigma_{\text{r}}(r)^2$ is dictated by the Jeans equation for density profiles that tend to a constant value, as may be readily ascertained by taking the derivative of $\rho(r)\sigma_{\text{r}}(r)^2$. To fix r_0, we will choose it to be equivalent to the Burkert scale radius where the density is one-fourth of the central density. The parameter ξ encapsulates uncertainties from the profile and velocity dispersion anisotropy in the outer parts of the halo. We test various models and find that a range of 2–3 for ξ is largely consistent with most parametrizations and hence we fix $\xi = 2.5$. If we specify the central velocity dispersion, then with an additional constraint on the core region (i.e. r_1), we would be able to back out both the core radius and the core density.

We then set $v_{\text{rms},0}^2$ equal to the average velocity dispersion squared (i.e. two times kinetic energy divided by mass) within the region r_1 in the absence of self-interactions. This basically demands that the kinetic energy within r_1 is unchanged from the value it would have had in the absence of self-interactions. Note, however, that we are setting the average velocity dispersion squared equal to $v_{\text{rms},0}^2$ and not the corresponding average in the SIDM halo. This is an approximation, but one that is degenerate with choosing the ξ parameter.

To finish specifying this model, we need a density profile for the region inside r_1. A Burkert profile has a velocity dispersion profile (assuming isotropy) that asymptotes very slowly to the central dispersion. For small radii, the radial dispersion profile is slowly increasing (with radius) because of the r/r_{b} term in the Taylor expansion for the density profile. If we want a flatter central dispersion profile (as is observed for the SIDM$_1$ haloes), we can fix this by either assuming an isothermal profile or something like $1/[1 + 1.52(r/r_0)^2]^{3/2}$. The final results turn out to be qualitatively similar for these profiles. Hence we adopt a Burkert profile for ease of comparison to the fits presented here and then check the results with more appropriate profiles later. Our two constraints (on the radial velocity dispersion and mass) fully specify the density and radial scales of the Burkert profile.

In order to obtain scaling relations we need to estimate r_1, which demarcates the inner region where self-interactions are effective from the outer region that is mostly undisturbed by the self-interactions. In reality, this divide will not be sharp but we will see that the main features of the scaling relations are well captured by this simple model. We define r_1 to be the region where each particle on average suffers one interaction. Since the region outside is assumed to be unperturbed by interactions, we may estimate r_1 as

$$\Gamma(r_1)t_{\text{age}} = 1.3\rho_{\text{CDM}}(r_1)v_{\text{rms,CDM}}(r_1)\frac{\sigma}{m}t_{\text{age}} = 1 \,, \tag{22}$$

where we set age (t_{age}) to be 10 Gyr for now, keeping in mind that larger haloes have a shorter age and that major mergers can reset the timer. We will consider what happens when t_{age} is a function of halo mass shortly. The factor 1.3 is $\langle|\boldsymbol{v} - \boldsymbol{u}|\rangle/\sqrt{\langle v^2\rangle}$ for a Maxwellian distribution where $\boldsymbol{u}$ and $\boldsymbol{v}$ are the velocities of the two interacting dark-matter particles. We have not attempted to use a more realistic velocity distribution since the dependence of this factor on a possible high-velocity cut-off to the distribution function was found to be fairly mild.

For the density profile in the absence of self-interactions, we assume an NFW profile and to fix the velocity dispersion we use the observed fact that the phase-space density is a power law in radius (Taylor & Navarro 2001). By noting that $v_{\text{rms, CDM}}(r) = [\rho_{\text{CDM}}(r)/Q(r)]^{1/3}$ and using a phase-space density profile $Q(r) = Q(r_{\text{s}})(r/r_{\text{s}})^{-\eta}$ (Taylor & Navarro 2001; Ascasibar et al. 2004; Rasia, Tormen & Moscardini 2004; Dehnen & McLaughlin 2005; Ascasibar & Gottlöber 2008), we may fully specify the dependence of r_1 on the cross-section and halo parameters (say V_{max} and r_{max}). For the phase-space density profile, we use a power-law index $\eta = 2$ and $Q(r_{\text{s}}) = 0.3/(GV_{\text{max}}r_{\text{max}}^2)$ derived from jointly fitting our relaxed CDM haloes; these parameters are very similar to the fits provided in Ascasibar & Gottlöber (2008).

Let us first look at how r_1 scales with r_{s} in the NFW density profile. One notes that $\rho_{\text{s}} = 1.72V_{\text{max}}^2/(Gr_{\text{max}}^2)$ and hence $\rho_{\text{s}}V_{\text{max}} \propto V_{\text{max}}^3/r_{\text{max}}^2$ which is a very mildly increasing function of V_{max} as equation (15) shows. Thus, equation (22) implies that r_1/r_{s} should be roughly a constant. Numerically, we find that $r_1/r_{\text{s}} \simeq 0.7-0.8$ over the range of V_{max} of interest for $\sigma/m = 1\,\text{cm}^2\,\text{g}^{-1}$.

Having now specified r_1, we are ready to look at the scalings of r_{b} and ρ_{b}. For our assumed value of ξ, $v_{\text{rms},0}^2 \simeq 2.5\,G\rho_{\text{b}}r_{\text{b}}^2$. Thus, we are looking for the value of $r_{\text{b}}/r_{\text{s}}$ that solves

$$\left\langle \frac{\rho_{\text{s}}}{(r/r_{\text{s}})(1 + r/r_{\text{s}})^2}\frac{(r/r_{\text{s}})^{\eta}}{Q(r_{\text{s}})} \right\rangle (r_1) = (v_{\text{rms},0})^3 \,, \tag{23}$$

with the constraint that $M_{\text{b}}(r_1) = M_{\text{NFW}}(r_1)$, where $M_{\text{NFW}}(r)$ and $M_{\text{b}}(r)$ are the masses enclosed within radius r for NFW and Burkert profiles, respectively. We note that if $r_{\text{b}}/r_{\text{s}}$ is not a strong function of V_{max} and since we know r_1/r_{s} is a mild function of V_{max}, then the mass constraint essentially sets $\rho_{\text{b}}r_{\text{b}}^3/(\rho_{\text{s}}r_{\text{s}}^3)$ to be a constant or $\rho_{\text{b}}r_{\text{b}}^3 \propto (\rho_{\text{s}}r_{\text{s}}^3)$. This implies $v_{\text{rms},0}^2r_{\text{b}} \propto V_{\text{max}}^2r_{\text{max}}$. Now equation (23) sets $v_{\text{rms, 0}} \simeq V_{\text{max}}$ because r_1/r_{s} is a mild function of V_{max} and it therefore follows that $r_{\text{b}} \propto r_{\text{s}}$ is a consistent solution to the above equations. As a check we note that assuming $r_1/r_{\text{s}} = 0.7-0.8$ gives $v_{\text{rms, 0}} \simeq 1.1V_{\text{max}}$, in reasonable agreement with our SIDM$_1$ simulation results (see Fig. 6). This simple model thus predicts that $r_{\text{b}}/r_{\text{s}}$ should not vary much with V_{max} in agreement with the observed scaling relations from the SIDM$_1$ simulation.

In detail, the model predicts that $r_{\text{b}}/r_{\text{s}} = 0.5-0.6$ for dwarf to cluster haloes in good agreement with the fits to our SIDM$_1$ haloes, but about 25 per cent smaller for $V_{\text{max}} \sim 100\,\text{km\,s}^{-1}$. It departs from the results of the simulation in predicting that $r_{\text{b}}/r_{\text{s}}$ increases gently with V_{max}, whereas Fig. 11 predicts that this ratio should decrease gently with V_{max}. We find that this departure from simulations is likely related to the assumption of a constant age for all haloes. To generalize our model, we use the results of Wechsler et al. (2002) who show that the virial concentrations of haloes are correlated with their formation times, and in particular $c_{\text{vir}} = 4.1(1 + z_{\text{form}})$ for a particular definition of formation time. We invert this equation to derive an estimate of the halo age using z_{form}. With the age thus specified in equation (22), we find that now $r_{\text{b}}/r_{\text{s}}$ decreases gently with V_{max} in substantial agreement with the fit to our simulations. Thus, the reason that larger haloes have a smaller $r_{\text{b}}/r_{\text{s}}$ is because self-interactions have had less time to operate. We note that the values for the core radius in the analytic model with halo mass-dependent t_{age} are uniformly about 25 per cent smaller, but this should not be a cause for concern given the approximation in demanding a sharp transition at r_1.

Given the Burkert core radius r_{b} and the central velocity dispersion $v_{\text{rms, 0}}$, one can easily check that the central density ρ_{b} is about $0.01\,\text{M}_{\odot}\,\text{pc}^{-3}$ for $V_{\text{max}} = 300\,\text{km\,s}^{-1}$ haloes and $0.005\,\text{M}_{\odot}\,\text{pc}^{-3}$ for $V_{\text{max}} = 1000\,\text{km\,s}^{-1}$ in this analytic model. These numbers and the

scaling with V_{max} for ρ_b (when including the halo mass-dependent t_{age}) are in good agreement with the densities in Fig. 12 and the fit in equation (19). As we have indicated before, the scaling relation for the central density should be interpreted with care given the large scatter. Given the tight correlation between core radius and r_s, it is possible that the substantial scatter in the central density arises in large part due to the scatter introduced by the assembly history in the concentration–mass relation. This has important implications for fitting to the rotation velocity profiles of low surface brightness spirals (LSBs; Kuzio de Naray et al. 2010) and deserves more work.

The simple model constructed above also provides insight into the core-collapse time-scales. In particular, as long as the outer part (region outside r_1) dominates the potential well and sets the average central temperature (or the total kinetic energy in the core), we do not expect core collapse. This is simply because core collapse requires uncontrolled decrease in temperature, which is prohibited here. Once r_1 moves out well beyond r_{max} or to the virial radius, there is significant loss of particles and core collapse may occur if there are no further major mergers. The time-scale for this process is much longer than the age of the Universe for $\sigma/m = 1\,\mathrm{cm^2\,g^{-1}}$ because the inner core is at $r_1 < r_s$ after 10 Gyr for this self-interaction strength and we see no evidence for significant mass loss.

8 OBSERVATIONAL COMPARISONS

The goal of this section is to discuss our results in comparison to observationally inferred properties of dark-matter density profiles. In particular, we will focus on the core densities and core sizes. Section 8.1 presents our expectations for SIDM$_1$ and SIDM$_{0.1}$. Our predictions for $\sigma/m = 1\,\mathrm{cm^2\,g^{-1}}$ are anchored robustly to our simulations, though they do require some extrapolation beyond the mass range directly probed by our simulations ($V_{max} = 130-860\,\mathrm{km\,s^{-1}}$). For $\sigma/m = 0.1\,\mathrm{cm^2\,g^{-1}}$ the predictions are much less secure because the associated core sizes are of the order of our resolution limit; thus, we rely on our analytic model more directly here. In Section 8.2, we discuss our predictions in light of observations of dark-matter haloes for a wide range of halo masses. In Section 8.3, we discuss our results on subhaloes in the context of past work and constraints on SIDM based on subhalo properties.

Before proceeding with this discussion we would like to clarify how we quantify core sizes. In this work, we have fit the $\sigma/m = 1\,\mathrm{cm^2\,g^{-1}}$ haloes with Burkert density profiles. However, many observational constraints on cores on galaxy scales come from fitting pseudo-isothermal density profiles with core size r_{pi} to data (e.g. Simon et al. 2005; Kuzio de Naray et al. 2008), although some constraints do come from Burkert modelling (Salucci et al. 2012). We found that pseudo-isothermal density profiles also give good fits to the inner regions of the SIDM$_1$ haloes, but Burkert fits are better because of that profile's $\rho \propto r^{-3}$ dependence at large radii. For a pseudo-isothermal density profile [$\propto 1/(r_c^2 + r^2)$], the density decreases to one-fourth the central density at 1.73 times its core radius r_c. Thus, as a crude approximation, one may convert the Burkert radius to the equivalent pseudo-isothermal core radius by multiplying by a factor of 0.58 ($r_c \simeq r_b/1.73$).

8.1 Predicted core sizes and central densities in SIDM

8.1.1 SIDM with $\sigma/m = 1\,cm^2\,g^{-1}$

The central properties of dark-matter haloes have been inferred from observations from tiny Milky Way dSph galaxies ($V_{max} \lesssim$

$50\,\mathrm{km\,s^{-1}}$) to galaxy clusters ($V_{max} \gtrsim 1000\,\mathrm{km\,s^{-1}}$). If we extrapolate the results from our set of SIDM$_1$ simulations using equations (16)–(20), we predict that SIDM haloes with $\sigma/m = 1\,\mathrm{cm^2\,g^{-1}}$ would have the following (Burkert) core sizes and central densities:

For galaxy clusters ($V_{max} \simeq 700-1000\,\mathrm{km\,s^{-1}}$),

$$r_b \simeq (95-155)\,\mathrm{kpc}; \ \rho_b \simeq (0.005-0.004)\,\mathrm{M_\odot\,pc^{-3}}. \qquad (23)$$

For low-mass spirals ($V_{max} \simeq 50-130\,\mathrm{km\,s^{-1}}$),

$$r_b \simeq (3-10)\,\mathrm{kpc}\ ; \ \rho_b \simeq (0.02-0.01)\,\mathrm{M_\odot\,pc^{-3}}. \qquad (23)$$

For dSph galaxies ($V_{max} \simeq 20-50\,\mathrm{km\,s^{-1}}$),

$$r_b \simeq (0.9-3)\,\mathrm{kpc}\ ; \ \rho_b \simeq (0.04-0.02)\,\mathrm{M_\odot\,pc^{-3}}. \qquad (23)$$

Although we cannot completely determine the scatter in our scaling relations due to low number statistics, it is important to note from Figs 10 and 12 that a scatter of at least a factor of 2 in core sizes, and at least a factor of 3 in central densities, is expected for a given V_{max}. We suspect that these differences are in large part a result of the diversity of merger histories of dark-matter haloes. Note that the $V_{max}-r_{max}$ and $Q(r_s)$ scalings assumed in the analytic model are the median values. The strong dependence of the SIDM halo profiles on these quantities makes it clear that the scatter in these relations will introduce significant scatter in the halo core sizes and core densities. Thus, the analytic model should also provide a simple way to understand (some of the) scatter seen for SIDM$_1$ halo properties. In future work, we will characterize the relation between the core properties and merger history in the context of a detailed discussion of the scatter in the scaling relations, especially on scales that we do not resolve with our current simulations.

8.1.2 SIDM with $\sigma/m = 0.1\,cm^2\,g^{-1}$

As discussed in Section 5.4, our SIDM$_{0.1}$ simulations are not well enough resolved to definitively measure a core radius for any of our haloes, much less define scatter in that quantity. Nevertheless, our best resolved systems do demonstrate some clear deviations from CDM and allow us to cautiously estimate individual core densities. Referring back to Fig. 4, we see that in our two best resolved cluster haloes (at $M_{vir} \simeq 10^{14}\,\mathrm{M_\odot}$) the SIDM$_{0.1}$ core densities approach $\sim 0.01\,\mathrm{M_\odot\,pc^{-3}}$ – each at least a factor of ~ 3 denser than their SIDM$_1$ counterparts. Similarly, in our Z12 Milky Way case, the SIDM$_{0.1}$ core density appears to be approaching $\sim 0.1\,\mathrm{M_\odot\,pc^{-3}}$ compared to $\sim 0.02\,\mathrm{M_\odot\,pc^{-3}}$ in the SIDM$_1$ case.

Given the lack of well-resolved halo profiles, it is worth appealing to the analytic model presented in Section 7 to estimate core radii for SIDM$_{0.1}$. Using exactly the same arguments (including the halo mass-dependent age), we find that $r_1/r_s \simeq 0.05-0.12$ in the 100–1000 km s^{-1} V_{max} range and a corresponding Burkert core radius $r_b/r_s \simeq 0.09-0.17$. We note that the Burkert radius is close to but slightly larger than r_1. It is important to keep in mind that in this analytic model we are only explicitly fitting the inner 'self-interaction zone' of $r < r_1$. This does not imply that the entire halo has to be well fit by the Burkert profile. Recall that a single-scale Burkert profile only works as well as it does for $\sigma/m = 1\,\mathrm{cm^2\,g^{-1}}$ because $r_b \approx r_s$, such that to a good approximation there is only one relevant length scale. For the smaller cross-section that we are now considering we expect the core and NFW scale radii to be widely separated, suggesting that a generic functional form for SIDM haloes should have two scale radii. A wide separation between the SIDM$_{0.1}$ core and r_s does appear to be consistent with the highest resolved haloes presented in Fig. 4. However, we note

that given the strong correlation between r_b/r_s, we still expect a one-parameter family of models for a given σ/m.

To see how dependent our results are on the shape of the *inner* halo profile, we modify the analytic model to include a density profile that decreases with radius as $1/[1+(r/r_c)^2]^{\alpha/2}$. For this density profile, the velocity dispersion profile has the right form to match our simulation results. The price we pay is the introduction of a new parameter α. We set this parameter α by additionally demanding that the slope of the mass profile (i.e. density) is continuous at r_1, so that the mass profile joins smoothly with the NFW mass profile. This picks out a narrow range $\alpha = 5.5-7.0$ as the solution over most of the V_{max} range of interest (with smaller values corresponding to lower V_{max}). Interestingly, this implies that at r_1, the slope of the density profile is very close to -2 for the entire range of V_{max} values of interest. Note that while the mass profile is continuous, the slope of the density profile is not matched smoothly at r_1 (since the slope of the NFW profile would be closer to -1 at $r_1 \ll r_s$). This probably signals that if the matching were not done sharply (at r_1), the density profile of SIDM would overshoot that of CDM and catch up at some radius beyond r_1 (as is seen in the comparison of $SIDM_1$ and CDM density profiles).

As a check we apply this α model to the $\sigma/m = 1$ cm^2 g^{-1} case and find that the results are qualitatively the same as the model with the Burkert profile. The quantitative differences are at 20 per cent level with the densities being smaller and inferred Burkert core radii (where density is one-fourth of the central density) larger compared to the Burkert profile model. The predicted slope of the density profile at r_1 is close to -2.5 implying a smoother transition to the NFW profile (since $r_1 \sim r_s$ for $\sigma/m = 1$ cm^2 g^{-1}), as is seen Fig. 4.

For the $\sigma/m = 0.1$ cm^2 g^{-1} case, we obtain $r_c/r_s = 0.08-0.17$ and an equivalent Burkert core radius (where the density is one-fourth of the central density) $r_b/r_s = 0.06-0.14$, in substantial agreement with the results we obtained using the Burkert profile. Thus, our analysis would suggest core sizes $\sim 0.1 r_s$ for $\sigma/m = 0.1$ cm^2 g^{-1}. The results from the analytic model for $\sigma/m = 0.1$ cm^2 g^{-1} also seem consistent with our simulation results; see Fig. 6 where the v_{rms} profiles for $SIDM_{0.1}$ start to deviate from CDM at $\sim 0.2 r_s$.

Based on the discussion above, we conclude that for $\sigma/m = 0.1$ cm^2 g^{-1} we expect the following:

For galaxy clusters ($V_{max} \simeq 700-1000$ km s^{-1}),

$$r_b \sim (16-20)\,\text{kpc};\ \rho_b \sim 0.04\,\text{M}_\odot\,\text{pc}^{-3}. \qquad (23)$$

For low-mass spirals ($V_{max} \simeq 50-130$ km s^{-1}),

$$r_b \sim (0.6-2.5)\,\text{kpc};\ \rho_b \sim 0.2-0.1\,\text{M}_\odot\,\text{pc}^{-3}. \qquad (23)$$

For dSph galaxies ($V_{max} \simeq 20-50$ km s^{-1}),

$$r_b \sim (0.2-0.6)\,\text{kpc};\ \rho_b \sim 0.5-0.2\,\text{M}_\odot\,\text{pc}^{-3}. \qquad (23)$$

These values do not include the scatter from mass assembly history. It is probably reasonable to assume a factor of 2 scatter for both core radii and core densities based on what we see in $SIDM_1$. It is also possible that the core densities are ~ 50 per cent smaller than what we would see in simulations, given that the $SIDM_1$ simulations have core densities that are somewhat larger than the predictions from the analytic model. For the dSph galaxies, the values should be interpreted with caution as it is the prediction for field haloes with V_{max} range 20–50 km s^{-1}.

While these values are somewhat tentative compared to those presented above for $SIDM_1$ (given our lack of direct simulation fits), two factors are reassuring. First, the analytic model is based on the simple assumption that scattering redistributes kinetic energy within the inner halo and the non-trivial aspect of the model is defining this 'inner halo' region. There is no reason to suspect that this assumption or the prescription breaks down for $SIDM_{0.1}$ haloes when it works so well in describing the $SIDM_1$ haloes. The predicted densities are in line with those inferred for the best resolved haloes in our $SIDM_{0.1}$ simulations (shown in Fig. 4 and discussed above). For the core radii, we reiterate that the label 'r_b' should be interpreted (according to its definition in the analytic model) as the radius where the density reaches one-fourth the asymptotic core density. The overall profile of a halo with such a small core compared to r_s will not be fit by the Burkert form. Note that the strong correlations we predict between the core radius and the NFW scale radius raise the intriguing possibility that the SIDM haloes may be also well fit (modulo scatter) by a single parameter profile as is the case for CDM.

Next, we compare our predictions for SIDM core properties against data and show that the core radii and densities appear to be consistent with that seen in real data, motivating future simulations with high enough resolution to resolve cores in $SIDM_{0.1}$ haloes.

8.2 Observed core sizes and central densities versus SIDM

In this section, we explore the predictions for the properties of density profiles with SIDM in the context of observational constraints on density profiles. We also revisit previous constraints on SIDM from observations in light of our simulation suite.

8.2.1 Clusters

One of the tightest SIDM constraints from the first generation of SIDM studies emerged from one cluster simulation and one observed galaxy cluster. Specifically, Yoshida et al. (2000) simulated an individual galaxy cluster with different SIDM cross-sections. When comparing the core size of this simulated cluster to the core size estimated by Tyson, Kochanski & dell'Antonio (1998) for CL 0024+1654, they found that the observed core in CL 0024+1654 would be consistent with SIDM only if $\sigma/m \lesssim 0.1$ cm^2 g^{-1}. Since that time, evidence has emerged that this particular cluster is undergoing a merger along the line of sight (Czoske et al. 2001, 2002; Zhang et al. 2005; Jee et al. 2007; Jee 2010; Umetsu et al. 2010). Thus, this cluster is not the ideal candidate for SIDM constraints based on the properties of relaxed haloes, and the Yoshida et al. (2000) constraint is not valid in this context.

Using X-ray emission, weak lensing, strong lensing, stellar kinematics of the brightest cluster galaxy (BCG) or some combination thereof, the mass distributions within a number of galaxy clusters have been mapped in the past decade. Arabadjis, Bautz & Garmire (2002) placed a conservative upper limit of 75 kpc on the size of any constant-density core, and an average density within the inner 50 kpc of ~ 0.025 M$_\odot$ pc^{-3} for a halo with an estimated mass $M \sim 4 \times 10^{14}$ M$_\odot$.

Sand et al. (2004), Sand et al. (2008), Newman et al. (2009) and Newman et al. (2011) all find central density profiles in clusters shallower than the NFW CDM prediction. The difference in the work between these authors and others is that they use stellar kinematics of the BCG to constrain the density profile of the cluster dark-matter halo on small scales. While this probe of the density profile is more sensitive on small scales than strong lensing is, proper inference of the dark halo properties depends on accurate modelling of the BCG density profile and equilibrium structure.

They have typically assumed a '*g*NFW' profile in order to constrain the central densities: $\rho(r) \propto 1/[x^g(1 + x)^{3 - g}]$ with $r = xr_s$ and the NFW form obtained when $g = 1$. The Newman et al. (2009, 2011) mass models of $M \sim 10^{15}\,\mathrm{M}_\odot$ clusters show average dark-matter central densities within 10 kpc of $\sim 0.03 - 0.06\,\mathrm{M}_\odot\,\mathrm{pc}^{-3}$ and r_s of the order of 100 kpc. Note that 10 kpc is typically the smallest radius our simulations can resolve.

Saha, Read & Williams (2006) and Saha & Read (2009) studied the mass structure of three cluster haloes from gravitational lensing and obtained density profiles that are consistent with $\rho \propto r^{-1}$ outside the inner $10 - 20$ kpc regions. Similarly, Morandi, Pedersen & Limousin (2010) and Morandi & Limousin (2012) find that the radial mass distribution of cluster dark-matter haloes is consistent with NFW predictions outside 30 kpc in projection. The CLASH multi-cycle treasury programme on the *Hubble Space Telescope* is finding many new strongly lensed galaxies in about a set of 25 massive clusters (Postman et al. 2012). Initial results from this programme show that the total density profile of these clusters (or total density minus the BCG), if modelled as spherically symmetric, is consistent with NFW predictions for the halo alone if the *g*NFW functional form is used in the fit (Zitrin et al. 2011; Coe et al. 2012; Umetsu et al. 2012). However, Morandi et al. (2010) and Morandi, Pedersen & Limousin (2011) find that spherical mass modelling of galaxy clusters typically results in an overestimate of the cuspiness of the density profile, although axially symmetric modelling is found to lead to underestimates (Meneghetti et al. 2007). Thus, the present status of the density profiles of the CLASH clusters is unclear and clearly an interesting data set to look forward to.

We note here a complexity involved in using the lensing results to constrain SIDM models. Lensing provides mass in cylinders along the line of sight and this 2D mass profile is sensitive to mass from a large range of radii. As an example, let us consider mass within 30 kpc in projection. If we were to do something extreme and create a zero-density core inside 30-kpc sphere, the differences in the 2D mass profile would be less than a factor of 2 for clusters in the $10^{14} - 10^{15}\,\mathrm{M}_\odot$ mass range. For SIDM$_{0.1}$, the differences are comparatively benign. Our analytic model predicts that differences relative to CDM at about $0.1r_s$ (which is $10 - 40$ kpc for $10^{14} - 10^{15}\,\mathrm{M}_\odot$ virial mass range) are 20–30 per cent, which implies that SIDM$_{0.1}$ surface mass density profiles are very similar to CDM on these scales. Moreover, for SIDM$_1$ the expected differences would be measurably large.

On a related technical note, we discourage the use of the *g*NFW functional form when thinking about models that deviate from the CDM paradigm. In the SIDM case, for $\sigma/m < 1\,\mathrm{cm}^2\,\mathrm{g}^{-1}$, there will generically be two scale radii: one is the NFW-like scale radius which is the result of hierarchical structure formation (Lithwick & Dalal 2011) and the second is the core radius from dark-matter self-scattering. For $\sigma/m = 1\,\mathrm{cm}^2\,\mathrm{g}^{-1}$, as we explained in detail in Section 7, the two scales are about the same. If most of the cluster data constrain the density profile beyond an SIDM core, as they may for weak lensing and X-ray studies, the *g*NFW or NFW fit is dominated by those data, and a core will not be 'detected' in the fit. In future work, we will simulate haloes with a broader range of σ/m and provide SIDM-inspired density profiles to the community.

The results discussed above seem to suggest that the density profile beyond about 25 kpc should be close to the predictions from the NFW profile. To test this we plot the average physical density within 25 kpc for well-resolved haloes in our CDM (black), SIDM$_{0.1}$ (green) and SIDM$_1$ (blue) simulations in Fig. 13. We see that for the most massive haloes, the $\sigma/m = 1\,\mathrm{cm}^2\,\mathrm{g}^{-1}$ run produces densities at 25 kpc that are $\sim 2 - 3$ times lower than their
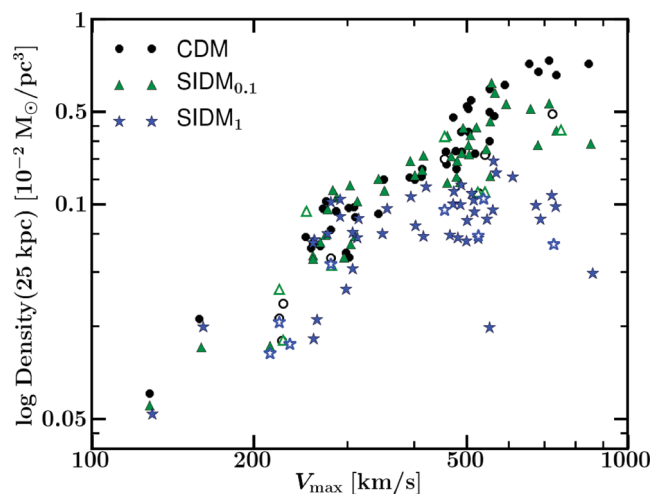

Figure 13. Dark-matter average density within 25 kpc versus V_{max} for resolved haloes in our CDM, SIDM$_{0.1}$ and SIDM$_1$ simulations. It is clear that SIDM$_1$ has significantly lower densities than CDM haloes at group and cluster scales. For the SIDM$_{0.1}$ model, the differences are muted and only appear on cluster scales. Thus, observations of central densities in clusters likely provide the most promising avenue to look for signatures of SIDM with cross-sections in the vicinity of 0.1 cm^2 g^{-1}.

CDM counterparts. Thus, it seems like the measured densities in clusters rule out the $\sigma/m = 1\,\mathrm{cm}^2\,\mathrm{g}^{-1}$ SIDM model. At the same time, the $\sigma/m = 0.1\,\mathrm{cm}^2\,\mathrm{g}^{-1}$ simulations are quite similar to CDM at these radii, though beginning to show some differences as we discussed earlier in this section. Analyses that combine information from X-rays, lensing and BCG stellar kinematics seem to suggest lowered densities (e.g. Newman et al. 2011) that would be compatible with SIDM$_{0.1}$. Given this outlook, it is reasonable to conclude that estimates of the central dark-matter density in clusters will provide essential tests of interesting SIDM models.

8.2.2 Low-mass spirals

For low-mass spirals with maximum circular velocities in the range $50 - 130\,\mathrm{km\,s}^{-1}$, constant-density cores with sizes of $\sim 0.5 - 8$ kpc and central densities of $\sim 0.01 - 0.5\,\mathrm{M}_\odot\,\mathrm{pc}^{-3}$ have been observed (de Blok et al. 2001; Sánchez-Salcedo 2005; Simon et al. 2005; Kuzio de Naray et al. 2008, 2010; Oh et al. 2011a; Salucci et al. 2012). Similar to what we found for cluster scales, SIDM with $\sigma/m = 1\,\mathrm{cm}^2\,\mathrm{g}^{-1}$ would be able to reproduce the *largest* core sizes observed in low-mass galaxies but it predicts central densities that are too low. SIDM with $\sigma/m = 0.1\,\mathrm{cm}^2\,\mathrm{g}^{-1}$ would be much more consistent. Moreover, the predicted log-slope of the density profile at 500 pc for $\sigma/m = 0.1\,\mathrm{cm}^2\,\mathrm{g}^{-1}$ haloes in the 50–130 km s^{-1} range is -0.5 to 0, both facts consistent with results from THINGS (Oh et al. 2011a). Note that the slope at 500 pc for the $\sigma/m = 1\,\mathrm{cm}^2\,\mathrm{g}^{-1}$ model is 0 in the same V_{max} range, which is not consistent with the scatter seen in the data.

We conclude, as before, that the observed densities and core radii are not consistent with SIDM$_1$ but are fairly well reproduced in SIDM models with $\sigma/m \simeq 0.1\,\mathrm{cm}^2\,\mathrm{g}^{-1}$.

8.2.3 Dwarf spheroidals in the Milky Way halo

The least massive and most dark-matter-dominated galaxies provide an excellent setting to confront the predictions of different dark-matter models with observations. Recent work by Boylan-Kolchin

et al. (2011, 2012) has found that the estimated central densities of the bright Milky Way dSph satellites are lower than the densities of the massive subhaloes in dark-matter-only simulations. SIDM offers a way to solve this problem because it reduces the central density of haloes. Thus in SIDM, the massive subhaloes *do* host the luminous dSph but have shallower density profiles than predicted in CDM simulations. This has recently been demonstrated by Vogelsberger et al. (2012). We do not directly compare to Vogelsberger et al. (2012) because their work is focused on the subhaloes of the Milky Way and the velocity-independent cross-section that they simulate ($\sigma/m = 10\,\text{cm}^2\,\text{g}^{-1}$) is larger than the cross-sections considered in our work.

Regardless of whether Milky Way dSphs have cuspy or cored dark-matter haloes, we may estimate the enclosed mass, and hence average density, around the half-light radius of the stellar distribution. Mass estimates within $300\,\text{pc}$ and mass profile modellings using stellar kinematics together with chemodynamically distinct stellar subcomponents of Milky Way dSph galaxies suggest central densities of $\sim 0.1\,\text{M}_\odot\,\text{pc}^{-3}$ (Strigari et al. 2008; Wolf et al. 2010; Walker & Peñarrubia 2011; Amorisco & Evans 2012; Wolf & Bullock 2012). For the faintest dSph Segue 1, the density within the half-light radius (about $40\,\text{pc}$) is measured to be about $2.5^{+4.1}_{-1.9}\,\text{M}_\odot\,\text{pc}^{-3}$ (Martinez et al. 2011; Simon et al. 2011). The errors on Segue 1 density are large but it is clear that if SIDM is to accommodate this result, it must allow for large scatter in the core sizes and densities for small $V_{\max}$ haloes. With a factor of 2–3 scatter in the densities quoted earlier for SIDM$_{0.1}$ haloes, Segue 1 would appear to be compatible with SIDM$_{0.1}$ if its $V_{\max}$ value is towards the lower end of the $20-50\,\text{km}\,\text{s}^{-1}$ range in $V_{\max}$.

For the two dSph galaxies that appear to have cored density profiles (Fornax and Sculptor), the core sizes must be of the order of $\sim 0.2-1\,\text{kpc}$ (Walker & Peñarrubia 2011). For small haloes with circular velocities in the $20-50\,\text{km}\,\text{s}^{-1}$ range, which is close to the expected peak circular velocities of dSph haloes before infall into the Milky Way host halo, an SIDM with $\sigma/m = 1\,\text{cm}^2\,\text{g}^{-1}$ predicts core sizes of the order of $\sim 0.8-3.0\,\text{kpc}$, with central densities of $\sim 0.02-0.04\,\text{M}_\odot\,\text{pc}^{-3}$. Therefore, we find again that $\sigma/m = 1\,\text{cm}^2\,\text{g}^{-1}$ cannot reproduce the observed high central densities. On the other hand, our estimates suggest that an SIDM model with $\sigma/m = 0.1\,\text{cm}^2\,\text{g}^{-1}$ would produce central densities and core sizes consistent with the Milky Way dSph.

In this last section we have used the analytic results that explain the scaling relations for the core sizes and central densities of haloes in our SIDM$_1$ and SIDM$_{0.1}$ simulations, to extrapolate our results to scales ranging from galaxy clusters to dSph galaxies and to lower cross-sections. We have found that $\sigma/m = 1\,\text{cm}^2\,\text{g}^{-1}$ would be unable to reproduce the observed high central densities. Remarkably, we find that the observations should be consistent with the predictions of an SIDM with cross-section in the ballpark of $\sigma/m = 0.1\,\text{cm}^2\,\text{g}^{-1}$. These expectations are based on the scaling relations seen in SIDM$_1$ simulations and our analytic model, which is consistent with the results from our direct $\sigma/m = 0.1\,\text{cm}^2\,\text{g}^{-1}$ simulations at the radii where we can trust our simulations. This deserves further study both in terms of simulations with SIDM cross-section values smaller than $1\,\text{cm}^2\,\text{g}^{-1}$ and more detailed comparisons to observations. Our current look at the global data does not suggest a need for a velocity-dependent cross-section as has been previously suggested. In a companion paper (Peter et al. 2012), we show that these SIDM models are also consistent with observations of halo shapes.

8.3 Observed substructure versus SIDM

In Fig. 8, we show that the number of subhaloes for $\sigma/m = 1\,\text{cm}^2\,\text{g}^{-1}$ is not significantly different from CDM predictions, especially in galaxy-scale haloes. This is interesting because it means that SIDM fails to deliver on one of the original motivations for considering this model of dark matter. Recall that Spergel & Steinhardt (2000) originally promoted SIDM as a solution to the missing satellites problem (Klypin et al. 1999; Moore et al. 1999), stating that many subhaloes would be evaporated by interactions with the background halo. Given the new discoveries of ultrafaint galaxies around the Milky Way and the high likelihood of many more discoveries from surveys like LSST (Bullock et al. 2010; Willman 2010), a significant reduction in substructure counts may very well be a negative characteristic of any non-CDM model (Tollerud et al. 2008).

However, in Milky Way mass haloes, SIDM with $\sigma/m = 1\,\text{cm}^2\,\text{g}^{-1}$ will yield a significant probability for subhalo particle scattering only for systems that pass within $\sim 10\,\text{kpc}$ of the host halo centre. Thus, for this cross-section, we can form interesting-sized cores but largely leave the subhalo mass function unaffected in Milky Way mass haloes. For smaller cross-sections, the differences between SIDM and CDM subhalo mass functions will be even smaller. We note that we are not the first to find that SIDM can form cores but not solve the missing satellites problem; it was first discussed in D'Onghia & Burkert (2003).

This finding is also interesting in the context of other alternatives to CDM. Warm dark matter (WDM) models, for which the outstanding difference from CDM is that dark-matter particles have high speeds at matter–radiation equality and a related free-streaming cut-off in the matter power spectrum, predict a suppression in the halo (and subhalo) mass function at small scales. Otherwise, the abundance and structure of haloes and subhaloes are nearly indistinguishable from CDM (Villaescusa-Navarro & Dalal 2011; Maccio' et al. 2012). WDM haloes may be less concentrated than CDM haloes on scales not much larger than the free-streaming scale, but are still *cusped*. They are only significantly cored right at the free-streaming scale, at which the halo and subhalo abundance is highly suppressed. Thus, each of the two leading modifications to CDM can solve only one of the two historical motivations for looking beyond the CDM paradigm.

The lack of subhalo suppression for $\sigma/m \lesssim 1\,\text{cm}^2\,\text{g}^{-1}$ has implications for another of the SIDM halo constraints from a decade ago. Gnedin & Ostriker (2001) set a constraint excluding the range of $0.3 < \sigma/m < 10^4\,\text{cm}^2\,\text{g}^{-1}$ based on the Fundamental Plane of elliptical galaxies. The argument rests on the observation that there are no significant differences in the Fundamental Plane of field and cluster ellipticals (e.g. Kochanek et al. 2000; Bernardi et al. 2003; La Barbera et al. 2010). Elliptical galaxies have a significant amount of dark matter within their half-light radii, with more massive ellipticals having larger mass-to-light ratios, either caused by varying stellar mass-to-light ratios or varying dark-matter content (Padmanabhan et al. 2004; Tollerud et al. 2011; Conroy & van Dokkum 2012). Gnedin & Ostriker (2001) argue that elliptical galaxies falling into cluster-mass haloes should have dark matter evaporated from their centres if $\sigma/m \neq 0$, which would cause the stars in the elliptical galaxy to adiabatically expand and hence move the galaxy off the Fundamental Plane.

However, in our simulations, we find that few subhaloes are fully evaporated, and that the subhalo $V_{\max}$ function is not greatly different for $\sigma/m = 1\,\text{cm}^2\,\text{g}^{-1}$ from CDM. In addition, our analytic arguments show that the trend with (host) halo mass for the

evaporation of subhaloes at fixed r/r_s is mild. This suggests that the Gnedin & Ostriker (2001) constraints are overly conservative even at the $\sigma/m \simeq 1$ cm^2 g^{-1} level. The main caveats are that the suppression of the subhalo V_{max} function is higher in more massive clusters and that the suppression is highest at the centre of the cluster halo. It would also be interesting to see if there are any differences in the Fundamental Plane as a function of projected distance in the cluster, both observationally and in simulations. For all of these reasons, it would be worthwhile to perform simulations of elliptical galaxies in clusters with SIDM and explore the Fundamental Plane constraints in more depth.

To summarize, although we have not fully resolved the cores of $\sigma/m = 0.1$ cm^2 g^{-1} SIDM haloes, the intuition gleaned from our analytic model (tested against the SIDM$_1$ results) and our moderately resolved simulation results suggest that $\sigma/m = 0.1$ cm^2 g^{-1} is an excellent fit to the data across the range of halo masses from dwarf satellites of the Milky Way to clusters of galaxies. Values of cross-section over dark-matter particle mass in this range are fully consistent with the *published* Bullet cluster constraints (cf. Section 1), measurements of dark-matter density on small scales and subhalo survival requirements. In a companion paper (Peter et al. 2012), we show that this model is also consistent with halo shape estimates. It is therefore important to simulate galaxy and cluster haloes with cross-sections in the 0.1 cm^2 g^{-1} range.

9 SUMMARY AND CONCLUSIONS

We have presented a new algorithm to include elastic self-scattering of dark-matter particles in *N*-body codes and used it to study the structure of SIDM haloes simulated in a full cosmological context. Our suite of simulations (summarized in Table 1) relies on identical initial conditions to explore SIDM models with velocity-independent cross-sections, $\sigma/m = 1$ and 0.1 cm^2 g^{-1} as well as a comparison set of standard CDM simulations (with $\sigma/m = 0$).

Our primary conclusion is that while SIDM looks identical to CDM on large scales, SIDM haloes have constant-density cores, with core radii that scale in proportion to the standard CDM scale radius ($r_{core} \simeq \epsilon \, r_s$). The relative size of the core increases with increasing cross-section ($\epsilon \simeq 0.7$ for $\sigma/m = 1$ and $\epsilon \sim 0.2$ for $\sigma/m = 0.1$ cm^2 g^{-1}). Correspondingly, at fixed halo mass, core densities decrease with increasing SIDM cross-section. For both core radii and core densities, there is significant scatter about the scaling with V_{max} of the halo. The scaling relationship is strong enough that measurements of dark-matter densities in the cores of dark-matter-dominated galaxies and large galaxy clusters likely provide the most robust constraints on the dark-matter cross-section at this time. In a companion paper (Peter et al. 2012) we demonstrate, in contrast to previous claims, that SIDM constraints from halo shape measurements may be less restrictive than (or at least similar to those from) measurements of absolute core densities alone.

Based on our simulation results, we conclude that the dark-matter self-scattering cross-section must be smaller than 1 cm^2 g^{-1} in order to avoid underpredicting the observed core densities in galaxy clusters, LSBs and dSph galaxies. However, an SIDM model with a *velocity-independent* cross-section of about $\sigma/m = 0.1$ cm^2 g^{-1} appears capable of reproducing reported core sizes and central densities of dwarfs, LSBs and galaxy clusters. Higher resolution simulations with better statistics will be needed to confirm this expectation.

An accounting of our results is as follows.

(i) Outside of the central regions of dark-matter haloes ($r \gtrsim 0.5R_{vir}$), the large-scale properties of SIDM cosmological simula-

tions are effectively identical to CDM simulations. This implies that all of the large-scale confirmations of the CDM theory apply to SIDM as well.

(ii) The subhalo V_{max} function in SIDM with $\sigma/m = 1$ cm^2 g^{-1} differs by less than $\sim$30 per cent compared to CDM across the mass range $5 \times 10^{11} - 2 \times 10^{14}$ M$_\odot$ studied directly with our simulations. Differences in the V_{max} function with respect to CDM are only apparent deep within the centres of large dark-matter haloes. Thus, although possible, it will be difficult to constrain SIDM models based on the effects of subhalo evaporation.

(iii) SIDM produces haloes with constant-density cores, with correspondingly lower central densities than CDM haloes of the same mass. For $\sigma/m = 1$ cm^2 g^{-1}, our simulated halo density structure is reasonably well characterized by a Burkert (1995) profile fit with a core size $r_b \simeq 0.7r_s$, where r_s is the NFW scale radius of the same halo in the absence of self-interactions. Core densities tend to increase with decreasing halo mass ($\rho_b \propto M_{vir}^{-0.2}$) but demonstrate about a factor of $\sim$3 scatter at fixed mass (likely owing to the intrinsic scatter in dark-matter halo concentrations).

(iv) SIDM halo core sizes, central densities and associated scaling relations can be understood in the context of a simple analytic model. The model treats the SIDM halo as consisting of a core region, where self-interactions have redistributed kinetic energy to create an approximately isothermal cored density profile; and an outer region, where self-interactions are not effective. The transition between these regions is set by the strength of the self-interactions and this model allows us to make quantitative predictions for smaller cross-sections where the cores are not resolved by our simulations. Based on this model and a few of our best resolved simulated haloes, we find core sizes $\sim$0.1r_s for $\sigma/m = 0.1$ cm^2 g^{-1}.

(v) Halo core densities over the mass range from 10^{15} to 10^{10} M$_\odot$ in SIDM with $\sigma/m = 1$ cm^2 g^{-1} are too low ($\sim$0.005–0.04 M$_\odot$ pc^{-3}) to match the observed central densities in galaxy clusters ($\sim$0.03 M$_\odot$ pc^{-3}) and dSphs ($\sim$0.1 M$_\odot$ pc^{-3}).

(vi) Halo core central densities in SIDM with $\sigma/m = 0.1$ cm^2 g^{-1} are in line with those observed from galaxy clusters to tiny dwarfs (0.02–0.5 M$_\odot$ pc^{-3}) without the need for any velocity dependence. The densities are more consistent with observations than those predicted in dissipationless CDM simulations, which are generically too high. SIDM models with this cross-section over dark-matter particle mass value are consistent with Bullet cluster observations, subhalo survival requirements and, as we show in a companion paper (Peter et al. 2012), measurements of dark-matter halo shapes.

Future work is necessary to expand both the dynamic range of our simulations in halo mass and resolution as well as the dynamic range in cross-sections. These simulations are necessary in order to make detailed comparisons with observations given the exciting possibility that dark-matter self-interaction with σ/m in the ballpark of 0.1 cm^2 g^{-1} could be an excellent fit to the central densities of haloes over 4–5 orders of magnitude in mass.

REFERENCES

Ackerman L., Buckley M. R., Carroll S. M., Kamionkowski M., 2009, Phys. Rev. D, 79, 023519
Ahn K., Shapiro P. R., 2005, MNRAS, 363, 1092
Amorisco N. C., Evans N. W., 2012, MNRAS, 419, 184
Arabadjis J. S., Bautz M. W., Garmire G. P., 2002, ApJ, 572, 66
Arkani-Hamed N., Finkbeiner D. P., Slatyer T. R., Weiner N., 2009, Phys. Rev. D, 79, 015014
Ascasibar Y., Gottlöber S., 2008, MNRAS, 386, 2022
Ascasibar Y., Yepes G., Gottlöber S., Müller V., 2004, MNRAS, 352, 1109
Balberg S., Shapiro S. L., Inagaki S., 2002, ApJ, 568, 475
Bernardi M. et al., 2003, AJ, 125, 1866
Boylan-Kolchin M., Bullock J. S., Kaplinghat M., 2011, MNRAS, 415, L40
Boylan-Kolchin M., Bullock J. S., Kaplinghat M., 2012, MNRAS, 422, 1203
Brook C. B., Stinson G., Gibson B. K., Roškar R., Wadsley J., Quinn T., 2012, MNRAS, 419, 771
Bullock J. S., 2010, arXiv e-prints
Bullock J. S., Kolatt T. S., Sigad Y., Somerville R. S., Kravtsov A. V., Klypin A. A., Primack J. R., Dekel A., 2001, MNRAS, 321, 559
Bullock J. S., Stewart K. R., Kaplinghat M., Tollerud E. J., Wolf J., 2010, ApJ, 717, 1043
Burkert A., 1995, ApJ, 447, L25
Burkert A., 2000, ApJ, 534, L143
Carlson E. D., Machacek M. E., Hall L. J., 1992, ApJ, 398, 43
Castignani G., Frusciante N., Vernieri D., Salucci P., 2012, arXiv e-prints
Coe D. et al., 2012, ApJ, 757, 22
Colín P., Avila-Reese V., Valenzuela O., Firmani C., 2002, ApJ, 581, 777
Conroy C., van Dokkum P., 2012, ApJ, 760, 71
Conroy C., Wechsler R. H., Kravtsov A. V., 2006, ApJ, 647, 201
Czoske O., Kneib J.-P., Soucail G., Bridges T. J., Mellier Y., Cuillandre J.-C., 2001, A&A, 372, 391
Czoske O., Moore B., Kneib J.-P., Soucail G., 2002, A&A, 386, 31
Davé R., Spergel D. N., Steinhardt P. J., Wandelt B. D., 2001, ApJ, 547, 574
de Blok W. J. G., 2010, Adv. Astron., 2010, 5
de Blok W. J. G., McGaugh S. S., Bosma A., Rubin V. C., 2001, ApJ, 552, L23
de Laix A. A., Scherrer R. J., Schaefer R. K., 1995, ApJ, 452, 495
Dehnen W., McLaughlin D. E., 2005, MNRAS, 363, 1057
D'Onghia E., Burkert A., 2003, ApJ, 586, 12
Dutton A. A. et al., 2011, MNRAS, 416, 322
Feng J. L., 2010, ARA&A, 48, 495
Feng J. L., Kaplinghat M., Tu H., Yu H.-B., 2009, J. Cosmol. Astropart. Phys., 7, 4
Feng J. L., Kaplinghat M., Yu H.-B., 2010, Phys. Rev. Lett., 104, 151301
Ferrero I., Abadi M. G., Navarro J. F., Sales L. V., Gurovich S., 2012, MNRAS, 425, 2817
Firmani C., D'Onghia E., Avila-Reese V., Chincarini G., Hernández X., 2000, MNRAS, 315, L29
Flores R. A., Primack J. R., 1994, ApJ, 427, L1

Gentile G., Salucci P., Klein U., Vergani D., Kalberla P., 2004, MNRAS, 351, 903
Gnedin O. Y., Ostriker J. P., 2001, ApJ, 561, 61
Governato F. et al., 2010, Nat, 463, 203
Governato F. et al., 2012, MNRAS, 422, 1231
Griest K., 1988, Phys. Rev. D, 38, 2357
Hahn O., Abel T., 2011, MNRAS, 415, 2101
Jee M. J., 2010, ApJ, 717, 420
Jee M. J. et al., 2007, ApJ, 661, 728
Jungman G., Kamionkowski M., Griest K., 1996, Phys. Rep., 267, 195
Katz N., White S. D. M., 1993, ApJ, 412, 455
Klypin A., Kravtsov A. V., Valenzuela O., Prada F., 1999, ApJ, 522, 82
Knollmann S. R., Knebe A., 2009, ApJS, 182, 608
Kochanek C. S., White M., 2000, ApJ, 543, 514
Kochanek C. S. et al., 2000, ApJ, 543, 131
Koda J., Shapiro P. R., 2011, MNRAS, 415, 1125
Komatsu E. et al., 2011, ApJS, 192, 18
Kravtsov A. V., Berlind A. A., Wechsler R. H., Klypin A. A., Gottlöber S., Allgood B., Primack J. R., 2004, ApJ, 609, 35
Kuzio de Naray R., Spekkens K., 2011, ApJ, 741, L29
Kuzio de Naray R., McGaugh S. S., de Blok W. J. G., 2008, ApJ, 676, 920
Kuzio de Naray R., Martinez G. D., Bullock J. S., Kaplinghat M., 2010, ApJ, 710, L161
La Barbera F., Lopes P. A. A., de Carvalho R. R., de La Rosa I. G., Berlind A. A., 2010, MNRAS, 408, 1361
Lithwick Y., Dalal N., 2011, ApJ, 734, 100
Loeb A., Weiner N., 2011, Phys. Rev. Lett., 106, 171302
Maccio' A. V., Paduroiu S., Anderhalden D., Schneider A., Moore B., 2012, MNRAS, 424, 1105
Machacek M. E., Carlson E. D., Hall L. J., 1993, Ann. New York Acad. Sci., 688, 681
Martinez G. D., Minor Q. E., Bullock J., Kaplinghat M., Simon J. D., Geha M., 2011, ApJ, 738, 55
Meneghetti M., Bartelmann M., Jenkins A., Frenk C., 2007, MNRAS, 381, 171
Miralda-Escudé J., 2002, ApJ, 564, 60
Monaghan J. J., Lattanzio J. C., 1985, A&A, 149, 135
Moore B., Ghigna S., Governato F., Lake G., Quinn T., Stadel J., Tozzi P., 1999, ApJ, 524, L19
Morandi A., Limousin M., 2012, MNRAS, 421, 3147
Morandi A., Pedersen K., Limousin M., 2010, ApJ, 713, 491
Morandi A., Pedersen K., Limousin M., 2011, ApJ, 729, 37
Natarajan P., Kneib J.-P., Smail I., Treu T., Ellis R., Moran S., Limousin M., Czoske O., 2009, ApJ, 693, 970
Navarro J. F., Frenk C. S., White S. D. M., 1997, ApJ, 490, 493
Newman A. B., Treu T., Ellis R. S., Sand D. J., Richard J., Marshall P. J., Capak P., Miyazaki S., 2009, ApJ, 706, 1078
Newman A. B., Treu T., Ellis R. S., Sand D. J., 2011, ApJ, 728, L39
Oh S.-H., de Blok W. J. G., Brinks E., Walter F., Kennicutt R. C., Jr, 2011a, AJ, 141, 193
Oh S.-H., Brook C., Governato F., Brinks E., Mayer L., de Blok W. J. G., Brooks A., Walter F., 2011b, AJ, 142, 24
Padmanabhan N. et al., 2004, New Astron., 9, 329
Peñarrubia J., Pontzen A., Walker M. G., Koposov S. E., 2012, ApJ, 759, L42
Peter A. H. G., 2012, arXiv e-prints
Peter A. H. G., Rocha M., Bullock J. S., Kaplinghat M., 2012, arXiv e-prints
Pontzen A., Governato F., 2012, MNRAS, 421, 3464
Pospelov M., Ritz A., Voloshin M., 2008, Phys. Lett. B, 662, 53
Postman M. et al., 2012, ApJS, 199, 25
Power C., Navarro J. F., Jenkins A., Frenk C. S., White S. D. M., Springel V., Stadel J., Quinn T., 2003, MNRAS, 338, 14
Randall S. W., Markevitch M., Clowe D., Gonzalez A. H., Bradač M., 2008, ApJ, 679, 1173
Rasia E., Tormen G., Moscardini L., 2004, MNRAS, 351, 237
Reddick R. M., Wechsler R. H., Tinker J. L., Behroozi P. S., 2012, arXiv e-prints
Reid B. A. et al., 2010, MNRAS, 404, 60

Rocha M., Peter A. H. G., Bullock J. S., 2012, MNRAS, 425, 231

Saha P., Read J. I., 2009, ApJ, 690, 154

Saha P., Read J. I., Williams L. L. R., 2006, ApJ, 652, L5

Salucci P., Burkert A., 2000, ApJ, 537, L9

Salucci P., Wilkinson M. I., Walker M. G., Gilmore G. F., Grebel E. K., Koch A., Frigerio Martins C., Wyse R. F. G., 2012, MNRAS, 420, 2034

Sánchez-Salcedo F. J., 2005, ApJ, 631, 244

Sand D. J., Treu T., Smith G. P., Ellis R. S., 2004, ApJ, 604, 88

Sand D. J., Treu T., Ellis R. S., Smith G. P., Kneib J.-P., 2008, ApJ, 674, 711

Simon J. D., Bolatto A. D., Leroy A., Blitz L., Gates E. L., 2005, ApJ, 621, 757

Simon J. D. et al., 2011, ApJ, 733, 46

Spergel D. N., Steinhardt P. J., 2000, Phys. Rev. Lett., 84, 3760

Springel V., 2005, MNRAS, 364, 1105

Steigman G., Turner M. S., 1985, Nucl. Phys. B, 253, 375

Strigari L. E., Bullock J. S., Kaplinghat M., Simon J. D., Geha M., Willman B., Walker M. G., 2008, Nat, 454, 1096

Taylor J. E., Navarro J. F., 2001, ApJ, 563, 483

Teyssier R., Pontzen A., Dubois Y., Read J., 2012, arXiv e-prints

Tollerud E. J., Bullock J. S., Strigari L. E., Willman B., 2008, ApJ, 688, 277

Tollerud E. J., Bullock J. S., Graves G. J., Wolf J., 2011, ApJ, 726, 108

Trujillo-Gomez S., Klypin A., Primack J., Romanowsky A. J., 2011, ApJ, 742, 16

Tyson J. A., Kochanski G. P., dell'Antonio I. P., 1998, ApJ, 498, L107

Umetsu K., Medezinski E., Broadhurst T., Zitrin A., Okabe N., Hsieh B.-C., Molnar S. M., 2010, ApJ, 714, 1470

Umetsu K. et al., 2012, ApJ, 755, 56

Villaescusa-Navarro F., Dalal N., 2011, J. Cosmol. Astropart. Phys., 3, 24

Vogelsberger M., Zavala J., Loeb A., 2012, MNRAS, 423, 3740

Walker M. G., Peñarrubia J., 2011, ApJ, 742, 20

Wechsler R. H., Bullock J. S., Primack J. R., Kravtsov A. V., Dekel A., 2002, ApJ, 568, 52

Willman B., 2010, Adv. Astron., 2010, 285454

Wolf J., Bullock J. S., 2012, arXiv e-prints

Wolf J., Martinez G. D., Bullock J. S., Kaplinghat M., Geha M., Muñoz R. R., Simon J. D., Avedo F. F., 2010, MNRAS, 406, 1220

Yoshida N., Springel V., White S. D. M., Tormen G., 2000, ApJ, 544, L87

Zhang Y.-Y., Böhringer H., Mellier Y., Soucail G., Forman W., 2005, A&A, 429, 85

Zitrin A. et al., 2011, ApJ, 742, 117

Zolotov A. et al., 2012, ApJ, 761, 71

APPENDIX A: DERIVATION OF THE HARD-SPHERE INTERACTION RATE IN *N*-BODY SIMULATIONS

The challenge is to represent a microphysical scattering process in a macroscopic context in which neither a fluid nor collisionless treatment is appropriate. In order to develop a Lagrangian technique in which to represent the scattering process, we start with the Boltzmann equation. Particles with mass m, a hard-sphere scattering cross-section $d\sigma/d\Omega$ (as a function of centre-of-mass scattering angle) and a distribution function $f(\boldsymbol{x}, \boldsymbol{v}, t)$ evolve as

$$\frac{Df(\boldsymbol{x}, \boldsymbol{v}, t)}{Dt} = \Gamma[f, \sigma] \tag{A1}$$

$$= \int d^3\boldsymbol{v}_1 \int d\Omega \frac{d\sigma}{d\Omega} |\boldsymbol{v} - \boldsymbol{v}_1| \left[f(\boldsymbol{x}, \boldsymbol{v}', t) f(\boldsymbol{x}, \boldsymbol{v}'_1, t) - f(\boldsymbol{x}, \boldsymbol{v}, t) f(\boldsymbol{x}, \boldsymbol{v}_1, t) \right]. \tag{A2}$$

Here, D/Dt is a Lagrangian time derivative and $\Gamma[f, \sigma]$ is the collision operator. If the particles were collisionless, the Lagrangian time derivative of the distribution function would be zero; the phase-space density of particles would be conserved. The left-hand expression in the brackets in equation (A2) represents scattering of particles into a small patch of phase space centred on $(\boldsymbol{x}, \boldsymbol{v})$, and the right-hand expression (after the minus sign) represents scattering out of that patch of phase space. If $\boldsymbol{v}$ and $\boldsymbol{v}_1$ represent the initial velocities of the primary and target particles, then $\boldsymbol{v}'$ and $\boldsymbol{v}'_1$ are their post-scatter velocities, which are related to the initial velocities by the centre-of-mass scattering angle Ω.

The key step in being able to represent the scattering process in a simulation is the ansatz that the evolution of the coarse-grained distribution function $\hat{f}$ (the distribution function averaged over several times the interparticle spacing) is a good representation of the evolution of the fine-grained distribution function f. In other words, the ansatz is that the solution to

$$\frac{D\hat{f}}{Dt} = \int d^3\boldsymbol{v}_1 \int d\Omega \frac{d\sigma}{d\Omega} |\boldsymbol{v} - \boldsymbol{v}_1| \left[\hat{f}(\boldsymbol{x}, \boldsymbol{v}', t) \hat{f}(\boldsymbol{x}, \boldsymbol{v}'_1, t) - \hat{f}(\boldsymbol{x}, \boldsymbol{v}, t) \hat{f}(\boldsymbol{x}, \boldsymbol{v}_1, t) \right] \tag{A3}$$

is the same as the solution for f in equation (A2) averaged over a patch of phase space. If this is the case, our next step is to discretize equation (A3) such that we can solve the Boltzmann equation by Monte Carlo N-body methods.

To discretize equation (A3), we consider a particle-based Lagrangian method in which each particle in the N-body simulation represents a patch of phase space. In the absence of collisions, the simulation particles trace out geodesics in the gravitational field of the particles. When we discretize the phase space, we do it as follows:

$$\hat{f}(\boldsymbol{x}, \boldsymbol{v}, t) = \sum_i (M_i/m) W(|\boldsymbol{x} - \boldsymbol{x}_i|; h_i) \delta^3(\boldsymbol{v} - \boldsymbol{v}_i). \tag{A4}$$

Here, i labels a discrete macroparticle representing a patch of phase space that has mass M_i; thus, each macroparticle represents a patch of phase space inhabited by M_i/m of the true particles. We assume a delta-function form for the velocity distribution because each macroparticle travels at only one speed. We treat each macroparticle as being smoothed out in configuration space with a smoothing kernel W with smoothing length h_i. The reason for treating each macroparticle as inhabiting a finite region of configuration space is that we want the local estimate of the density

$$n(x) = \int d^3\boldsymbol{v} \hat{f} \tag{A5}$$

to be smooth. Preliminary tests show that smoothness is necessary to properly estimate the collision term of the Boltzmann equation. Note that in the main text we use $M_i = m_p$ and $h_i = h_{si}$ for all i. This is because all of the N-body particles have the same mass in our simulations and we have fixed h_{si} to be constant for all particles in the simulations we present.

In the particle-based discretization of the Boltzmann equation, the fact that each particle represents a patch of phase space means that we must discretize the collision operator; we must integrate the collision operator over the patch of phase space inhabited by a single particle. Thus, if a specific particle represents a patch of phase space of size $\delta \boldsymbol{x}_p \delta \boldsymbol{v}_p$, we must calculate

$$\int_{\delta x_p} d^3\boldsymbol{x} \int_{\delta v_p} d^3\boldsymbol{v} \frac{D\hat{f}}{Dt} = \int_{\delta x_p} d^3\boldsymbol{x} \int_{\delta v_p} d^3\boldsymbol{v} \int d^3\boldsymbol{v}_1 \int d\Omega \frac{d\sigma}{d\Omega} |\boldsymbol{v} - \boldsymbol{v}_1| \left[\hat{f}(\boldsymbol{x}, \boldsymbol{v}', t)\hat{f}(\boldsymbol{x}, \boldsymbol{v}_1', t) - \hat{f}(\boldsymbol{x}, \boldsymbol{v}, t)\hat{f}(\boldsymbol{x}, \boldsymbol{v}_1, t) \right] . \quad \text{(A6)}$$

Thus, our approach to estimating the collision term and the Boltzmann equation is as follows. To find the collision *rate* for the region of phase space associated with a particle j, we divide equation (A6) by M_j/m (so that we are calculating the scattering probability for a single macroparticle j), and we consider only the 'scattering out' part of the collision operator. We consider the pairwise *rate* Γ_{ij} for particle j to scatter off any of the other i particles. We do a Monte Carlo simulation of the scatters; if a pair of particles is allowed to scatter in a given small time step, we calculate the macroparticles' post-scatter velocity using the centre-of-mass scattering angle Ω. This latter step is our approximation to the 'scatter out' term of the Boltzmann collision operator.

The pairwise collision operator is

$$\Gamma_{pq} = \frac{\Gamma(p|q) + \Gamma(q|p)}{2}, \quad \text{(A7)}$$

where the conditional probability of scattering a specific particle p off a target particle q is $\Gamma(q|p)$, which is determined by the collision term of the Boltzmann equation. This collision term is derived from equation (A6), such that

$$\Gamma(p) = \int_{\delta x_p} d^3\boldsymbol{x} \int_{\delta v_p} d^3\boldsymbol{v} \int d^3\boldsymbol{v}_1 \int d\Omega \frac{d\sigma}{d\Omega} |\boldsymbol{v} - \boldsymbol{v}_1| (M_p/m)^{-1} \hat{f}(\boldsymbol{x}, \boldsymbol{v}, t)\hat{f}(\boldsymbol{x}, \boldsymbol{v}_1, t) \quad \text{(A8)}$$

$$= \int_{\delta x_p} d^3\boldsymbol{x} \int_{\delta v_p} d^3\boldsymbol{v} \int d^3\boldsymbol{v}_1 \int d\Omega \frac{d\sigma}{d\Omega} |\boldsymbol{v} - \boldsymbol{v}_1| (M_p/m)^{-1} \left\{ \sum_j (M_j/m)W(|\boldsymbol{x} - \boldsymbol{x}_j|; h_j)\delta^3(\boldsymbol{v} - \boldsymbol{v}_j) \right.$$

$$\left. \sum_q (M_q/m)W(|\boldsymbol{x} - \boldsymbol{x}_q|; h_q)\delta^3(\boldsymbol{v}_1 - \boldsymbol{v}_q) \right\} \quad \text{(A9)}$$

$$= \int_{\delta x_p} d^3\boldsymbol{x} \int d^3\boldsymbol{v}_1 \int d\Omega \frac{d\sigma}{d\Omega} |\boldsymbol{v}_p - \boldsymbol{v}_1| \sum_q (M_q/m)W(|\boldsymbol{x} - \boldsymbol{x}_p|; h_p)W(|\boldsymbol{x} - \boldsymbol{x}_q|; h_q)\delta^3(\boldsymbol{v}_1 - \boldsymbol{v}_q) \quad \text{(A10)}$$

$$= \sum_q \int d\Omega \frac{d\sigma}{d\Omega} \frac{M_q}{m} |\boldsymbol{v}_q - \boldsymbol{v}_p| \int_{\delta x_p} d^3\boldsymbol{x} W(|\boldsymbol{x} - \boldsymbol{x}_p|; h_p)W(|\boldsymbol{x} - \boldsymbol{x}_q|; h_q) \quad \text{(A11)}$$

$$= \sum_q (\sigma/m)M_q|\boldsymbol{v}_q - \boldsymbol{v}_p|g_{pq} \quad \text{(A12)}$$

$$= \sum_q \Gamma(q|p). \quad \text{(A13)}$$

We note the appearance of the term σ/m, which is the scattering cross-section per unit mass. The kernel g is defined as

$$g_{pq} = \int_0^{\max(h_p, h_q)} d^3\boldsymbol{x}' W(|\boldsymbol{x}'|, h_p)W(|\delta\boldsymbol{x}_{pq} + \boldsymbol{x}'|, h_q). \quad \text{(A14)}$$

Using these sets of equations, we calculate Γ_{pq} for each pair of particles whose configuration-space patches overlap at each time step δt, making sure to keep the time steps small enough that $\Gamma_{pq}\delta t \ll 1$ for each time step.

APPENDIX B: TEST FOR THE SCATTERING KINEMATICS

We use the same set-up as described in Section 3 to test our implementation against the expected kinematics. For this we looked at the distributions of the post-scatter velocity magnitudes and directions for both the sphere and background particles. For the distributions of the velocity directions, we looked at the inclination and azimuthal angles of the post-scatter velocity vectors. The angles are defined such as the line of interaction is along the $\theta = 0$ direction (i.e. the z-axis) and ϕ is the azimuthal angle about which the experiment is symmetric. The distributions resulting from our test simulation are compared to those obtained from the transformation of a uniform isotropic distribution in the centre-of-mass frame to the simulation/lab frame; the results are shown in Figs B1–B3. Fig. B1 shows that the distributions of the velocity magnitudes rise linearly from $v = 0$ to v_s, followed by a sharp cut-off at $v = v_s$, where v_s is the relative speed between the sphere and the background. From conservation of energy, it is only possible to have particles with $v > v_s$ if they have interacted multiple times. Multiple interactions are not considered in our calculations of the theoretical distributions but they are allowed in our simulation; hence, in Fig. B1 one can observe a tail for velocities $> v_s$ on the distributions of both types of particle velocities, but not on the theoretical distribution. Looking at Fig. B2 one can see that most of the particles are scattered towards the $\theta = 45°$ directions, i.e. forming a $45°$ angle with respect to $\boldsymbol{v}_s$. It is visible that the distributions resulting from the simulation in the left-hand panel of Fig. B2 are higher than expected for $\theta \lesssim 20°$. This is again from the fact that multiple scatters are possible in the simulation and this is not included in the calculations of the theoretical histograms.
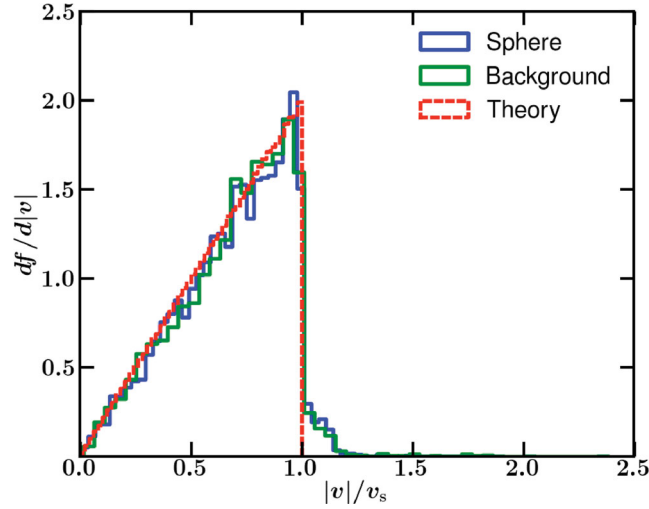
Figure B1. Distribution of the post-scatter velocity magnitudes. From conservation of energy it is only possible to have particles with velocities $>v_s$ if they have interacted multiple times, this is not included in our calculation of the theoretical distribution but it is allowed in our simulation, hence one can observe a tail for velocities $>v_s$ on the distributions of both types of particle velocities, but not on the theoretical distribution.
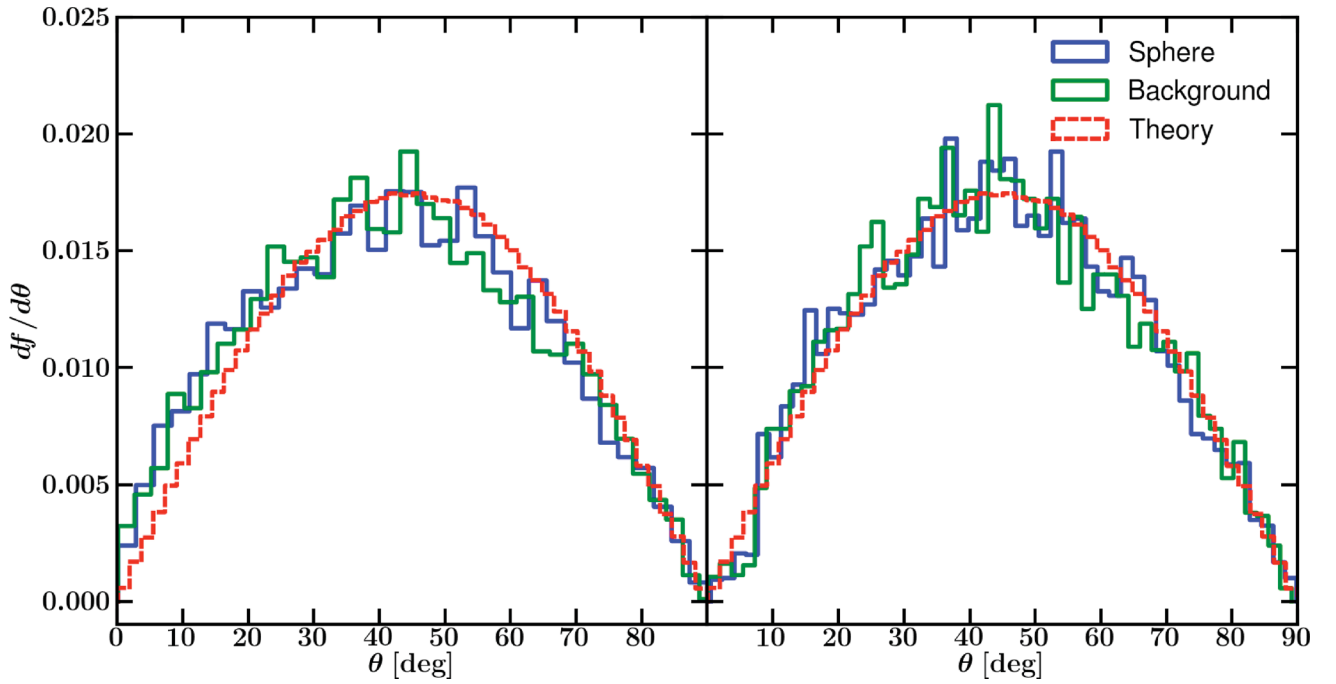

Figure B2. Distributions of the post-scatter velocities along the θ directions. It is evident that most of the particles are scattered towards the $\theta = 45°$ directions, i.e. forming a $45°$ angle with $\boldsymbol{v}_s$. Note that the distributions resulting from the simulation in the left-hand panel are higher that expected for $\theta \lesssim 20°$. This is because multiple scatters are possible in the simulation and they are not considered in the calculations of the theoretical histograms. We demonstrate this by showing in the right-hand panel the distributions from the simulation when we exclude any particles with $v > v_s$, excluding that way any particles that we know have interacted multiple times and bringing the distributions from the simulation to a better agreement with the theory.

We demonstrate that this is the case by showing in the right-hand panel of Fig. B2 the distributions obtained from the simulation when we exclude any particles with $v > v_s$, excluding that way any particles that we know have interacted multiple times, as one can see doing this brings the distributions from the simulation to a better match with the theory. Fig. B3 shows the distributions of the velocities as a function of ϕ, these are flat as expected due to the symmetry of the experiment.
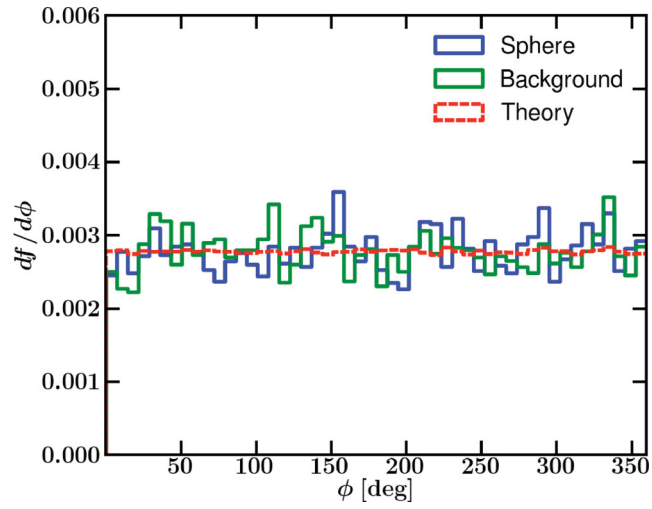
Figure B3. Distributions of the velocities along the ϕ directions. The flat distributions show that the results are symmetric about the direction of motion, i.e. the *z*-axis.

This paper has been typeset from a TEX/LATEX file prepared by the author.